Supplementary Information

Highly efficient water-splitting electrodes with stable operation at 3 A cm^{-2} in alkaline media through molecular linker assembly-induced all-in-one structured NiMo and NiFe electrocatalysts

Youhyun Son [a], Jeongmin Mo [a], Euiju Yong [a], Jeongyeon Ahn [a], Gyuchan Kim [b], Wonyoung Lee [b], Cheong Hoon Kwon [c], Hyun Ju [d], Seung Woo Lee [d], Byung-Hyun Kim [e,f,*], Myeongjin Kim [b,*], Jinhan Cho [a,g,h,*]

[a] *Department of Chemical and Biological Engineering, Korea University, 145 Anam-ro, Seongbuk-gu, Seoul 02841, Republic of Korea.*

[b] *Department of Hydrogen & Renewable Energy, Kyungpook National University, 80 Daehakro, Bukgu, Daegu 41566, Republic of Korea.*

[c] *Department of Energy Resources and Chemical Engineering, Kangwon National University, Samcheok, 25913, Republic of Korea*

[d] *The George W. Woodruff School of Mechanical Engineering Georgia Institute of Technology, Atlanta, GA 30332, USA.*

[e] *Department of Chemical and Molecular Engineering, Hanyang University ERICA, 55 Hanyangdaehak-ro, Sangnok-gu, Ansan-si, Gyeonggi-do 15588, Republic of Korea*

[f] *Department of Applied Chemistry, Center for Bionano Intelligence Education and Research, Hanyang University ERICA, 55 Hanyangdaehak-ro, Sangnok-gu, Ansan-si, Gyeonggi-do 1558 8, Republic of Korea*

[g] *KU-KIST Graduate School of Converging Science and Technology, Korea University, 145 Anam-ro, Seongbuk-gu, Seoul 02841, Republic of Korea*

[h] *Soft Hybrid Materials Research Center, Advanced Materials Research Division, Korea Institute of Science and Technology (KIST), Seoul 02792, Republic of Korea*

* Corresponding authors.

E-mail addresses: bhkim@kier.re.kr (B.-H. Kim), myeongjinkim@knu.ac.kr (M. Kim), jinhan71@korea.ac.kr (J. Cho)

Supplementary detailed experimental procedures

1. QCM Analysis

In QCM analysis, the relationship between Δm and ΔF can be described by the Sauerbrery equation (1) as follows [S1].

$$\Delta F(Hz) = -\frac{2F_0^2}{A\sqrt{\rho_q \mu_q}} \cdot \Delta m \qquad (1)$$

herein, F_0 (~ 5 MHz) refers to fundamental resonance frequency of the crystal, and A represents the surface area (cm^2) of an electrode. Additionally, ρ_q and μ_q denote mass density (2.65 g cm^{-3}) and shear modulus (2.95×10^{11} g cm^{-1} s^{-2}), respectively. After substituting these parameters, the equation (1) can be simplified to the following equation (2):

$$\Delta F(Hz) = -56.6 \cdot \Delta m \qquad (2)$$

2. Preparation of the Pt/C Ni foam electrode

Pt/C-coated Ni foam electrode was prepared by dispersing 1 mg Pt/C (20 wt.% Pt on Vulcan XC-72) in 300 μL of ethanol solution with 10.5 μL of 5 wt.% Nafion [S2]. The resulting catalyst dispersion was drop-casted onto a commercial Ni foam (0.5×0.5 cm^2), and then dried at room temperature for 8 h under vacuum condition.

3. Preparation of the IrO_2 Ni foam electrode

IrO_2-coated Ni foam electrodes were prepared by dispersing 1 mg IrO_2 in 300 μL of ethanol solution with 10.5 μL of 5 wt.% Nafion [S2]. Specifically, the IrO_2 catalyst-containing solution was drop-casted onto a commercial Ni foam (0.5×0.5 cm^2) using the same method as described above for the Pt/C Ni foam electrode. The IrO_2-coated Ni foam was then dried at room temperature for 8 h under vacuum condition.

4. Computational Methods

Density functional theory (DFT) calculations were performed using Vienna ab initio simulation software package (VASP) [S3-S6]. The electron exchange-correlation functionals were adopted by the generalized gradient approximation (GGA) using the Perdew-Burke-Ernzerhof (PBE) method [S7]. The projector augmented wave (PAW) method [S8, S9] was used for the explicit treatment of valence electrons with a plane wave cutoff energy of 500 eV. The convergence criteria of energy and maximum force are 10^{-6} eV and 0.02 eV/Å, respectively. For Ni and NiMo model structures, we considered Ni (111) metal slabs consisting of five atomic layers with the 4 × 4 supercells. A vacuum region of 15 Å normal to the surface was introduced to suppress the undesired image-image interactions due to the periodic boundary conditions. The bottom two layers were fixed to mimic a thick bulk layer while the rest of the atoms were allowed to fully relax. The Brillouin zones were sampled using the Monkhorst-Pack scheme [S10] with 2 × 2 ×1 *k*-points.

The surface free energy is calculated as

$$\gamma = (E_{\mathrm{tot}} - n_{\mathrm{Ni}}E_{\mathrm{Ni}} - n_{\mathrm{Mo}}E_{\mathrm{Mo}})/2A \qquad (3)$$

where γ is the surface free energy of the metal alloy slab, E_{tot} is the total energy of the relaxed metal alloy slab, A is the surface area of the model, n_{atom} and E_{atom} are the number of atoms in the slab model and the energy of one atom in the bulk structure, respectively.

The Gibbs free energy of HER and OER were calculated as follows:

$$\Delta G_{\mathrm{ads}} = \Delta E_{\mathrm{ads}} + \Delta E_{\mathrm{ZPE}} - T\Delta S \qquad (4)$$

where ΔE_{ads} is the DFT-calculated adsorption energy of HER and OER adsorbate, ΔE_{ZPE} is the zero-point energy difference between the adsorbate and the gas phase of adsorbate, and $T\Delta S$ is the entropic contribution to the free energy.

For both Ni-LDH and NiFe-LDH structures, a $Ni(OH)_2$ framework with a (011) orientation was employed as the host structure. Specifically, for NiFe-LDH, a Fe atom was substituted for the surface-exposed Ni to focus explicitly on the effects of Fe substitution. The Hubbard correction proposed by Dudarev et al. was used to accurately treat the Ni and Fe 3d states with a U-value of 6.6 eV and 3.5 eV on the Ni and Fe 3d states, respectively [S11,S12].

Under alkaline conditions, the oxygen evolution reaction proceeds through the following four steps:

$$* + OH^- \rightarrow *OH + e^- \quad (5)$$

$$*OH + OH^- \rightarrow *O + H_2O(l) + e^- \quad (6)$$

$$*O + OH^- \rightarrow *OOH + e^- \quad (7)$$

$$*OOH + OH^- \rightarrow * + O_2(g) + H_2O(l) + e^- \quad (8)$$

where * represents the active site on each catalyst, and *OH, *O, and *OOH are adsorption intermediates of the OER, respectively.

5. Carbon corrosion test

For carbon corrosion test (*in-situ* gas analysis) of OER electrodes, a mass spectrometer (Cirrus 2, MKS Instruments) was connected to the electrochemical cell in series. Ar gas (ultrahigh purity, Airgas) was fed into the electrochemical cell as a carrier gas (flow rate of 20 mL min^{-1}) controlled by a mass flow controller (G-series, MKS Instruments) [S13].

6. Calculation of faradaic efficiency

Faradaic efficiency of water splitting was calculated using the results measured by a eudiometer in an experimental setup. For this, the working electrode was fixed inside an inverted burette filled with electrolyte. Entire metal wires used for connecting the working electrode were coated

with insulating epoxy to prevent charge loss from side reactions. The evolved gases were directly collected in the headspace of the inverted burette, and the corresponding gas volume was determined by the displacement of the vertical water column. Based on this method, Faradaic efficiency was calculated by comparing the amount of evolved gas with the theoretically calculated amount of gas based on the charge passed through the electrode:

$$\text{Faradaic efficiency } (H_2) = \frac{V_{experiment}}{V_{theoretical}} = \frac{V_{experiment}}{\frac{2}{4}\times\frac{Q}{F}\times V_m} \qquad (9)$$

$$\text{Faradaic efficiency } (O_2) = \frac{V_{experiment}}{V_{theoretical}} = \frac{V_{experiment}}{\frac{1}{4}\times\frac{Q}{F}\times V_m} \qquad (10)$$

where F is the Faraday constant (96,485 C mol^{-1}), Q is the total amount of the charge passed through the electrodes, the number 4 represents 4 moles of electrons per mole of H_2O, the number 2 represents 2 moles of H_2 per mole of H_2O, the number 1 represents 1 mole of O_2 per mole of H_2O and V_m is the molar volume of gas (24.5 L mol^{-1}, 298 K, 101 kPa) [S14].

Supplementary figures

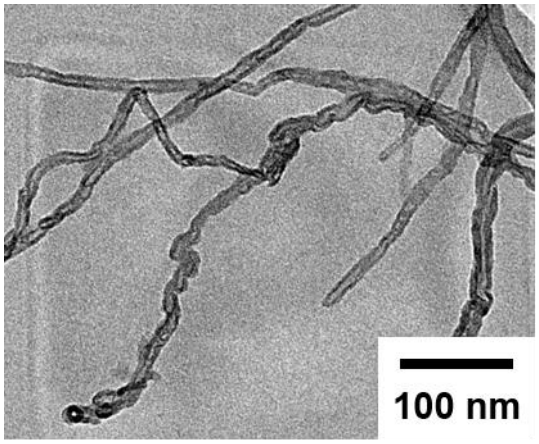

Fig. S1. HR-TEM image. HR-TEM image of COOH-MWCNT.

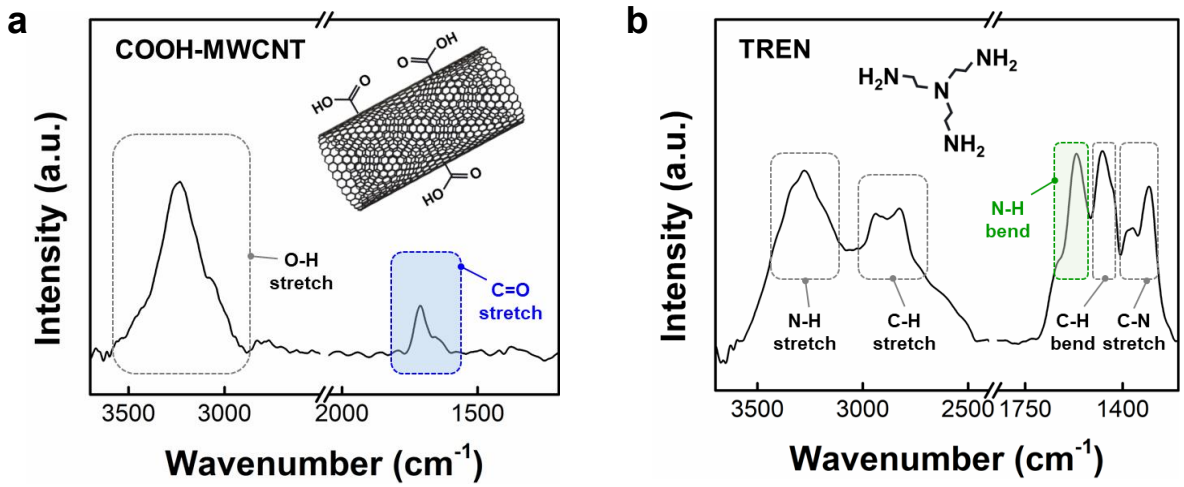

Fig. S2. Preparation of COOH-MWCNTs. FTIR spectra of (a) COOH-MWCNT and (b) TREN. The insets show the molecular structure of COOH-MWCNT and TREN.

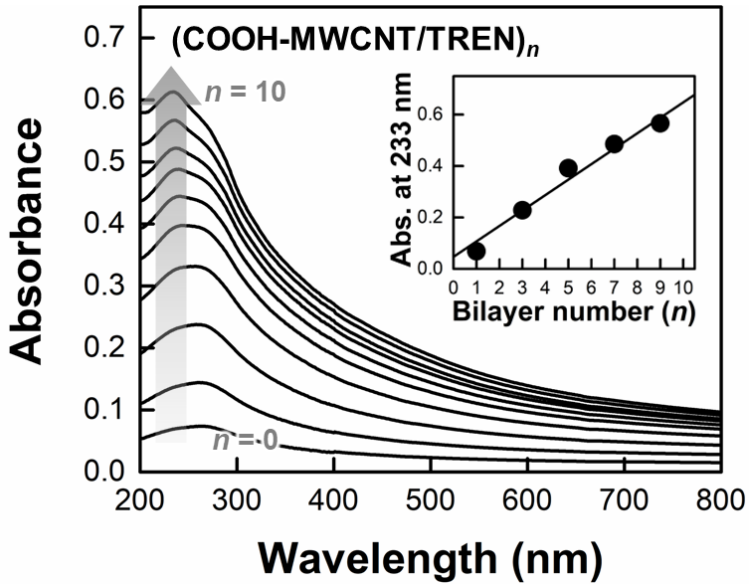

Fig. S3. UV-vis spectroscopy data. UV-vis spectra of (COOH-MWCNT/TREN)$_n$ multilayers as a function of bilayer number (n).

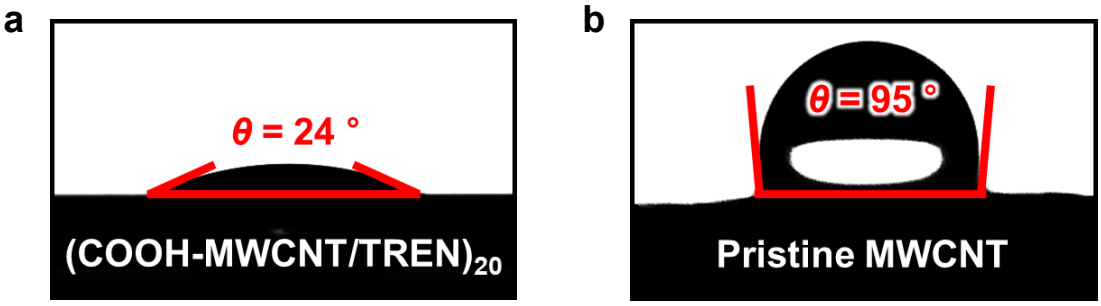

Fig. S4. Water contact angle measurement. Water contact angle of (a) (COOH-MWCNT/TREN)$_{20}$ multilayer-coated Si wafer and (b) pristine MWCNT-casted onto Si wafer using N-Methyl-2-pyrrolidone solvent.

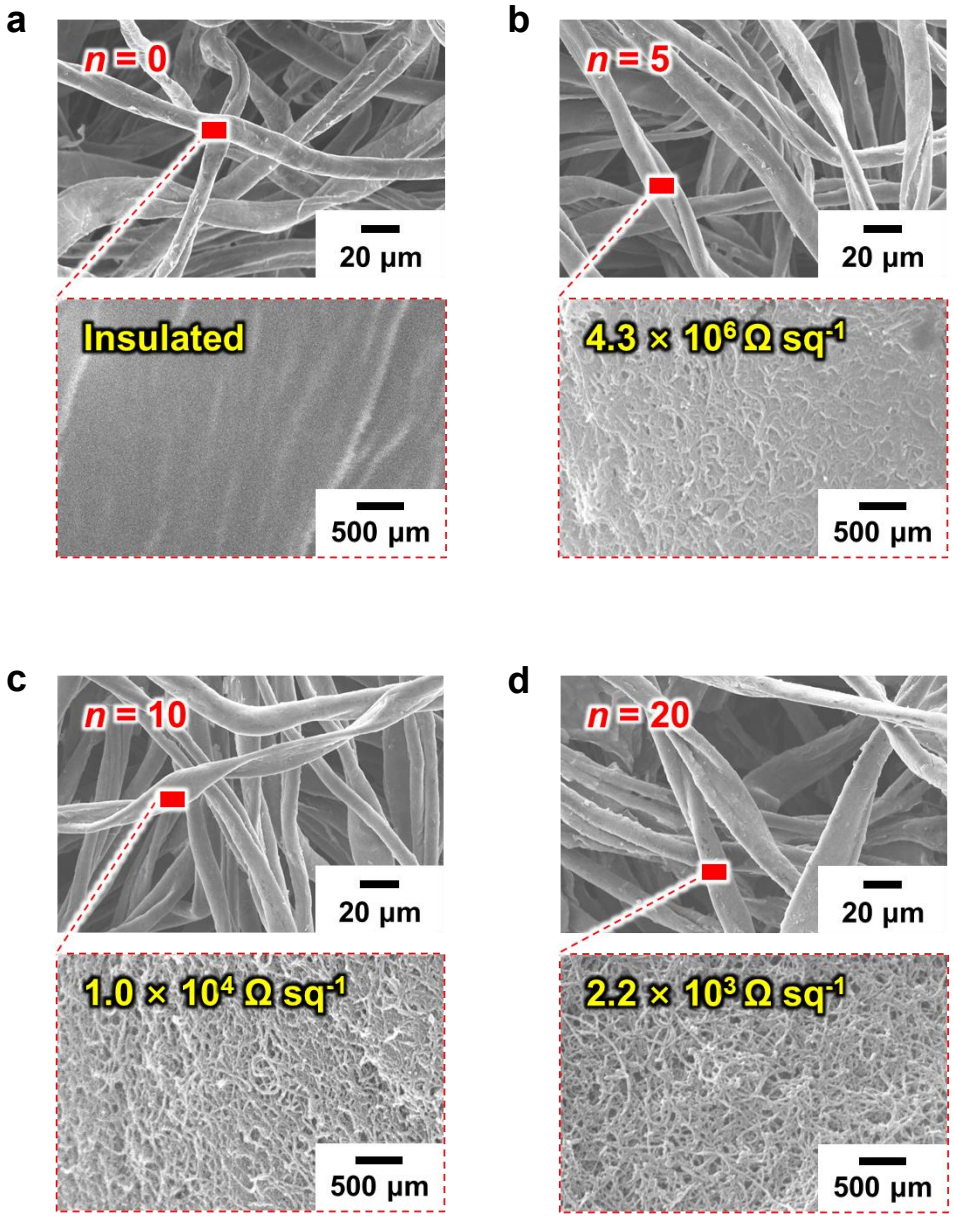

Fig. S5. FE-SEM images of COOH-MWCNT-based textile. FE-SEM images of $(\text{COOH–MWCNT/TREN})_n$ multilayer-coated textile with different bilayer number (n). (a) n = 0, (b) n = 5, (c) n = 10, and (d) n = 20.

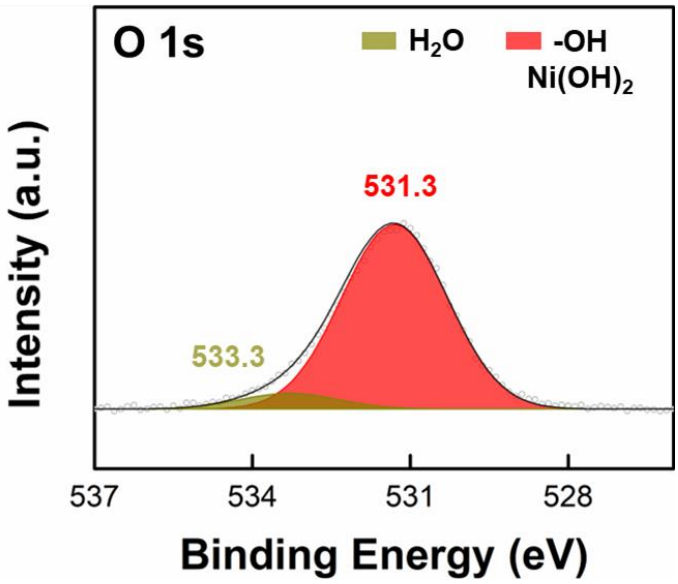

Fig. S6. XPS analysis. O 1s XPS spectra of Ni–ED CTT

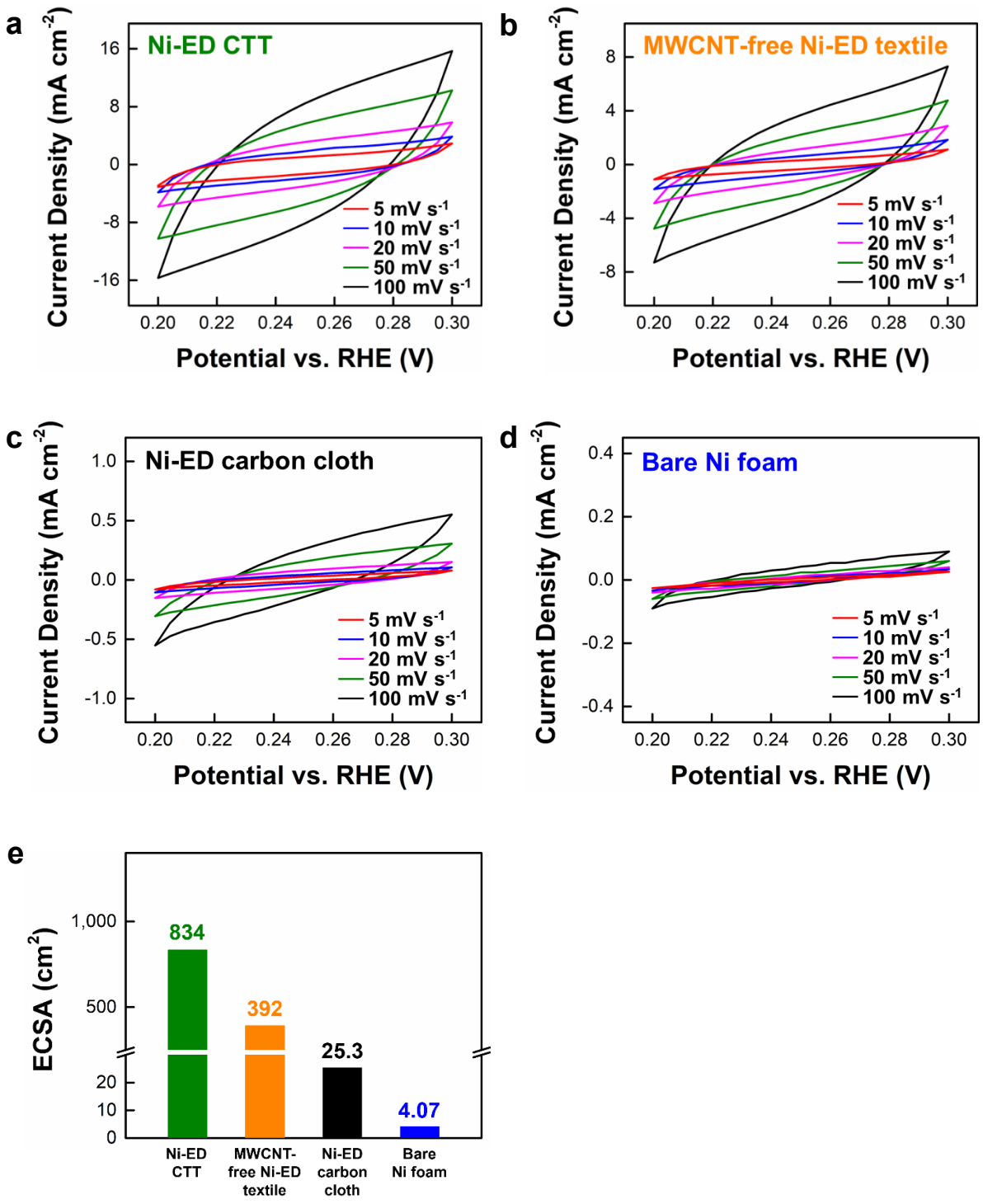

Fig. S7. CV and ECSA measurements. CV curves for (a) Ni-ED CTT, (b) MWCNT-free Ni-ED textile, (c) Ni-ED carbon cloth, and (d) bare Ni foam. These CV curves were recorded in the non-faradaic region (0.2–0.3 V) at different scan rates (5, 10, 20, 50, and 100 mV s^{-1}). (e) ECSA values for each electrodes calculated from C_{dl} (double-layer capacitance) based on

following equation:

$$ECSA = C_{dl}/C_s \times GSA$$

in here, C_s is specific capacitance of Ni (40 μF cm^{-2}) and GSA means geometric surface area of an electrode.

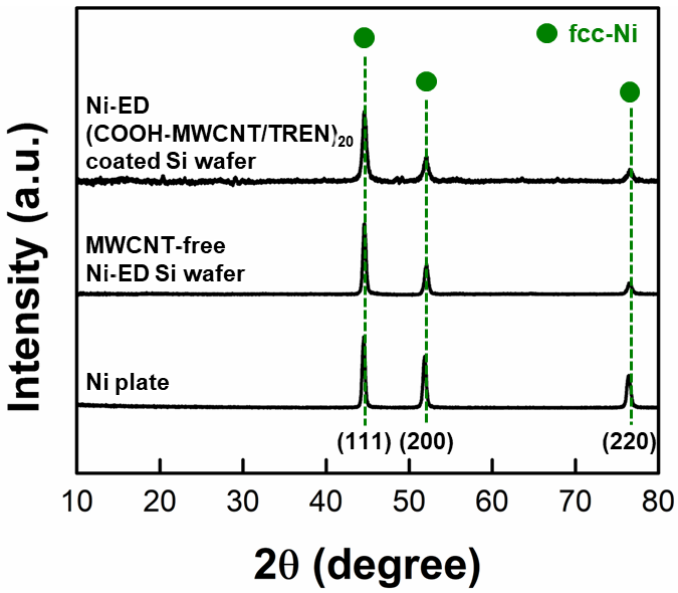

Fig. S8. XRD analysis. XRD patterns of Ni electrodeposited (COOH–MWCNT/TREN)$_{20}$ multilayer-coated Si wafer, Ni electrodeposited MWCNT-free Si wafer, and bare Ni plate.

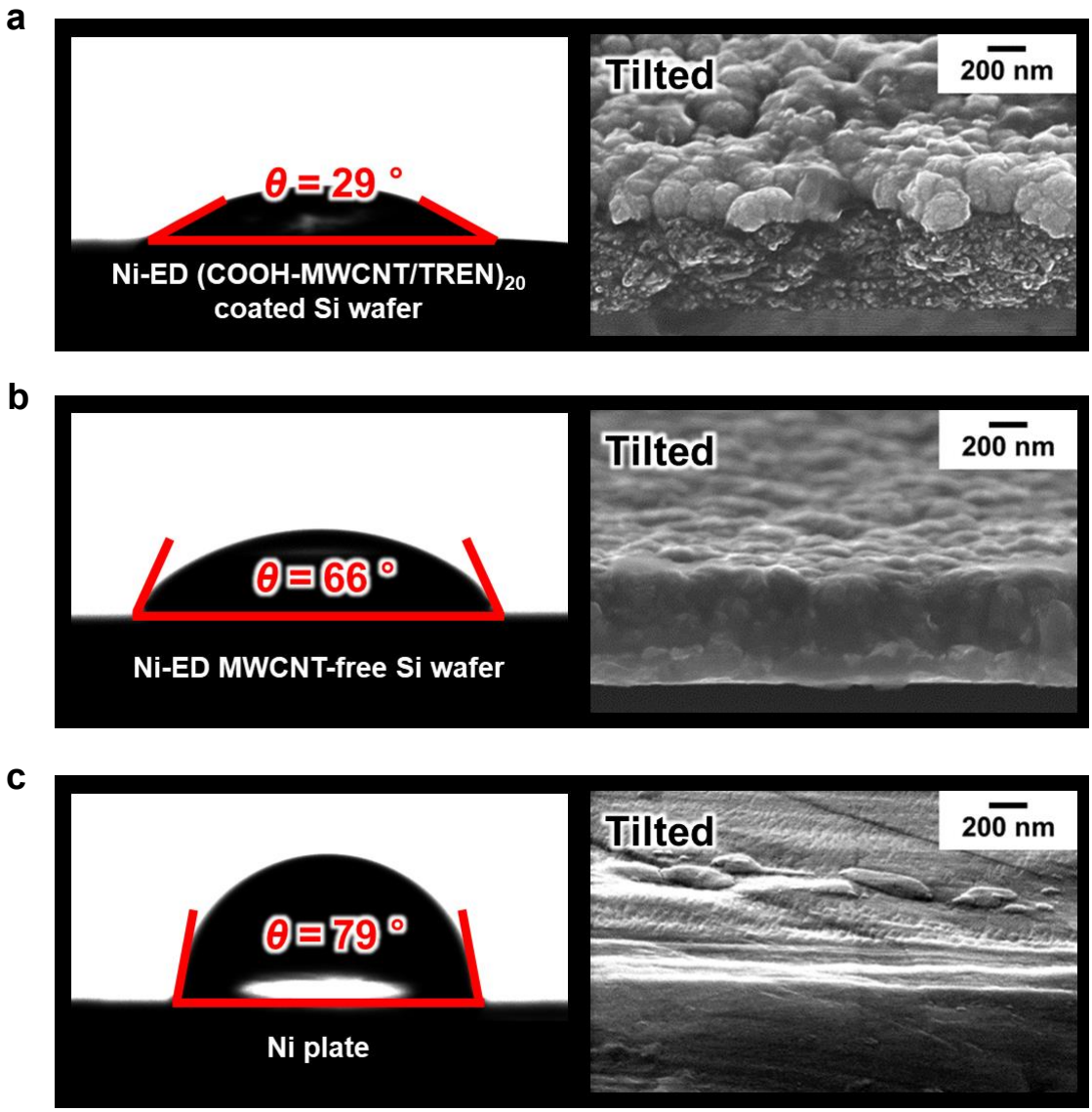

Fig. S9. Water contact angles and FE-SEM images. Water contact angle and tilted (40˚) FE-SEM images of (a) Ni-electrodeposited (COOH–MWCNT/TREN)$_{20}$ multilayer-coated Si wafer, (b) Ni-electrodeposited MWCNT-free Si wafer, and (c) bare Ni plate.

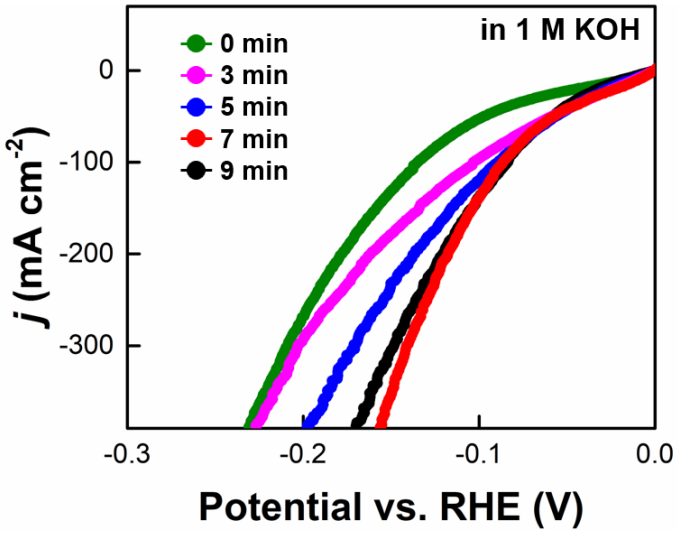

Fig. S10. HER polarization curves. The HER polarization curves of the NiMo-ED CTT with different electrodeposition time.

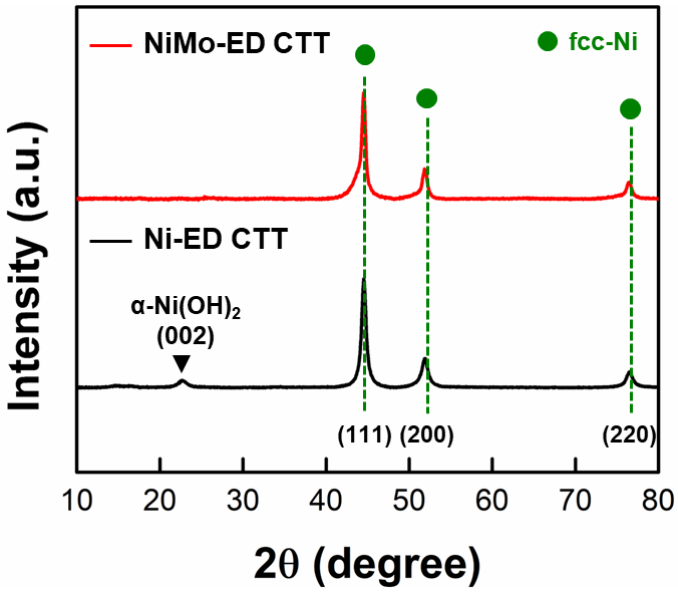

Fig. S11. XRD analysis. XRD patterns of NiMo–ED CTT and Ni-ED CTT

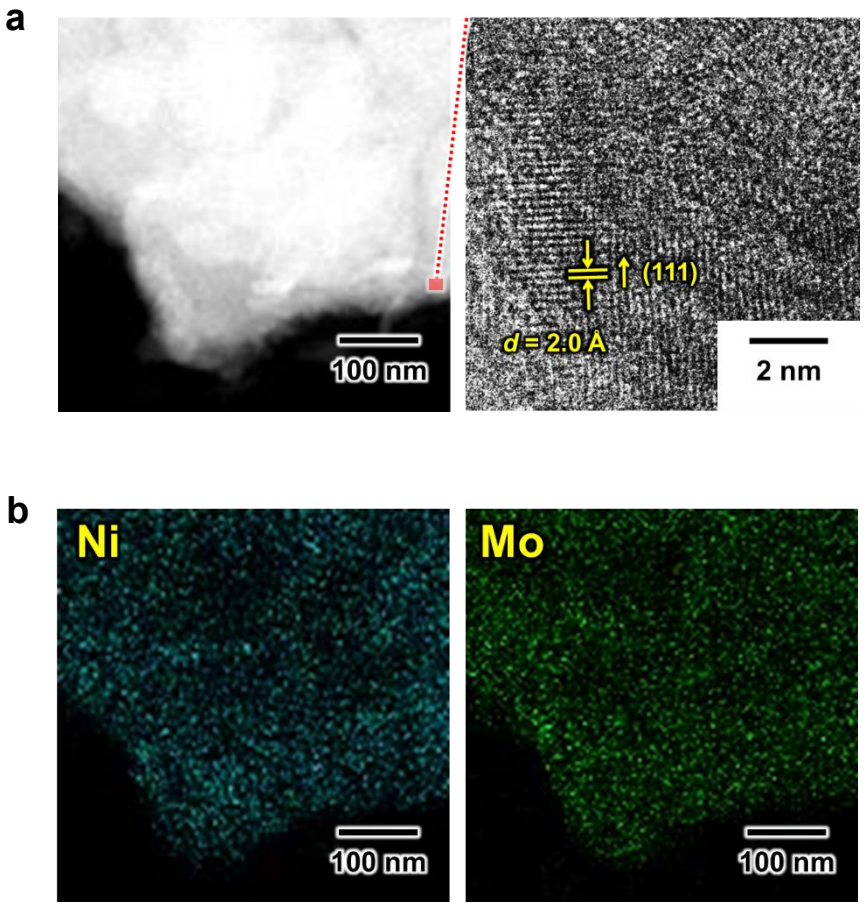

Fig. S12. HR-TEM and EDS mapping images. (a) HR-TEM images and (b) its corresponding EDS mapping of NiMo-ED CTT.

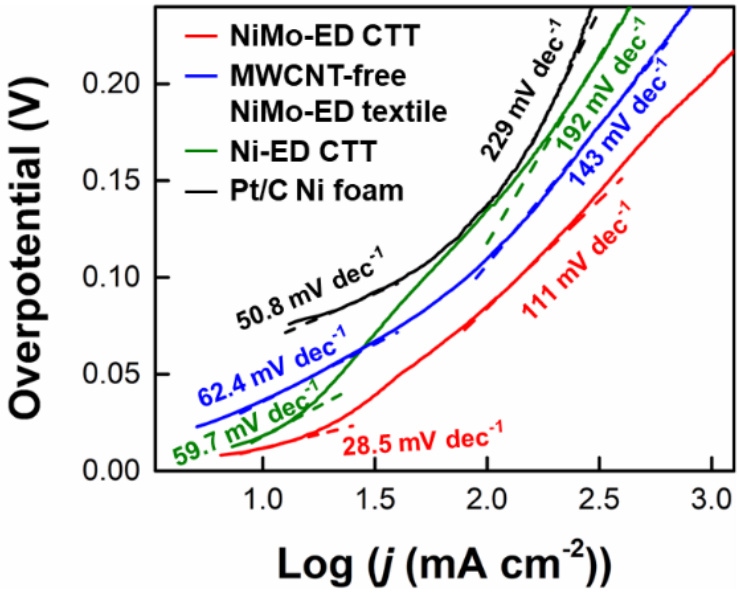

Fig. S13. Tafel plots. Tafel plots for the for NiMo-ED CTT versus MWCNT-free NiMo-ED textile, Ni-ED CTT, and Pt/C Ni foam. In lower overpotential area, NiMo-ED CTT exhibited a Tafel slope of 28.5 mV dec^{-1} and followed the reation with a Tafel step as the rate-determining step (RDS). In contrast, each electrode showed a Tafel slope of around 120 mV dec^{-1} in the high over potential region, indicating that the Volmer step acts as the RDS for HER.

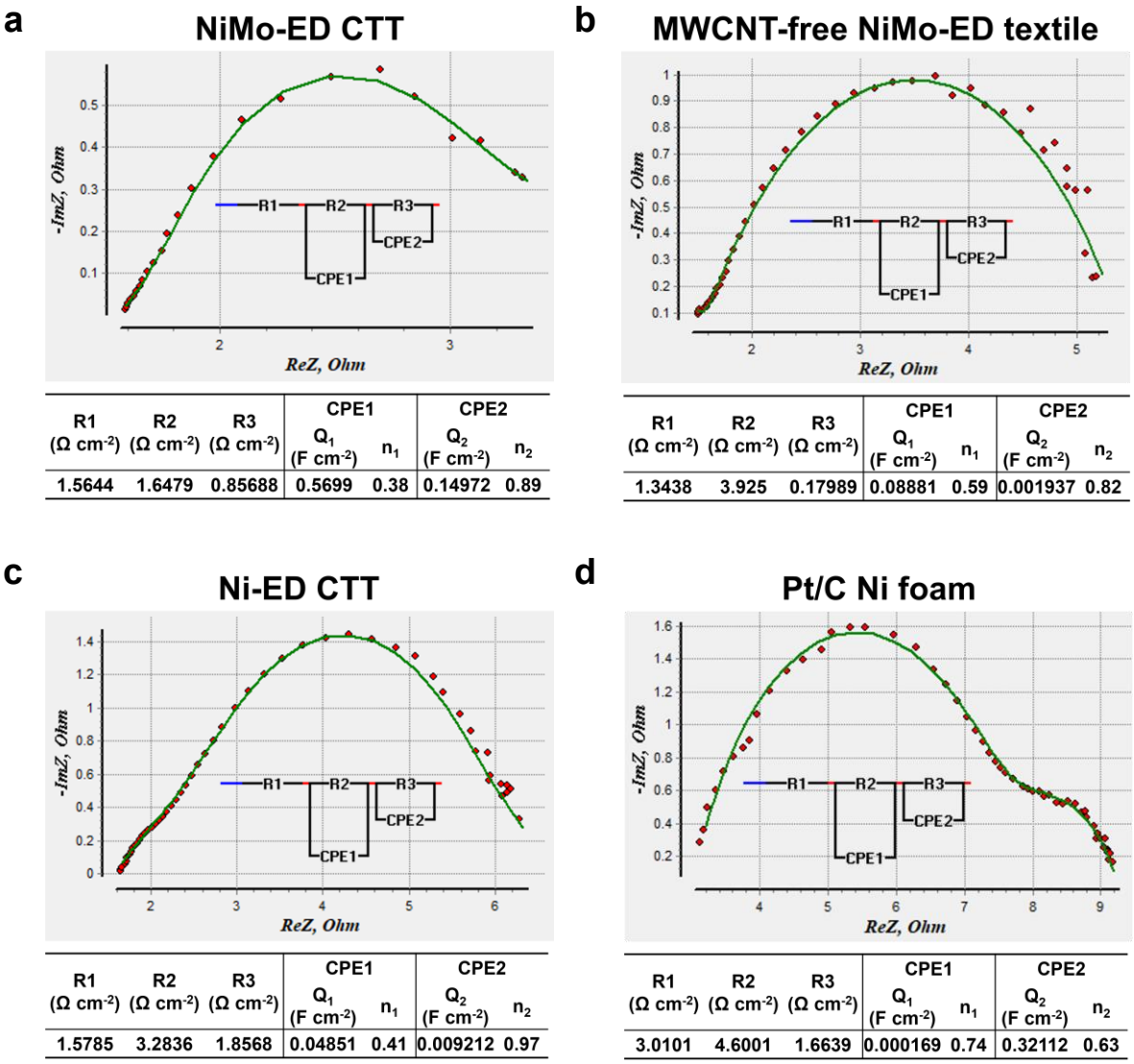

R1 (Ω cm^{-2})	R2 (Ω cm^{-2})	R3 (Ω cm^{-2})	CPE1 Q_1 (F cm^{-2})	CPE1 n_1	CPE2 Q_2 (F cm^{-2})	CPE2 n_2
1.5644	1.6479	0.85688	0.5699	0.38	0.14972	0.89

R1 (Ω cm^{-2})	R2 (Ω cm^{-2})	R3 (Ω cm^{-2})	CPE1 Q_1 (F cm^{-2})	CPE1 n_1	CPE2 Q_2 (F cm^{-2})	CPE2 n_2
1.3438	3.925	0.17989	0.08881	0.59	0.001937	0.82

R1 (Ω cm^{-2})	R2 (Ω cm^{-2})	R3 (Ω cm^{-2})	CPE1 Q_1 (F cm^{-2})	CPE1 n_1	CPE2 Q_2 (F cm^{-2})	CPE2 n_2
1.5785	3.2836	1.8568	0.04851	0.41	0.009212	0.97

R1 (Ω cm^{-2})	R2 (Ω cm^{-2})	R3 (Ω cm^{-2})	CPE1 Q_1 (F cm^{-2})	CPE1 n_1	CPE2 Q_2 (F cm^{-2})	CPE2 n_2
3.0101	4.6001	1.6639	0.000169	0.74	0.32112	0.63

Fig. S14. EIS plots of HER electrodes. EIS plots of (a) NiMo–ED CTT, (b) MWCNT-free NiMo-ED textile, (c) Ni-ED CTT, and (d) Pt/C-Ni foam with the corresponding equivalent circuit (inset).

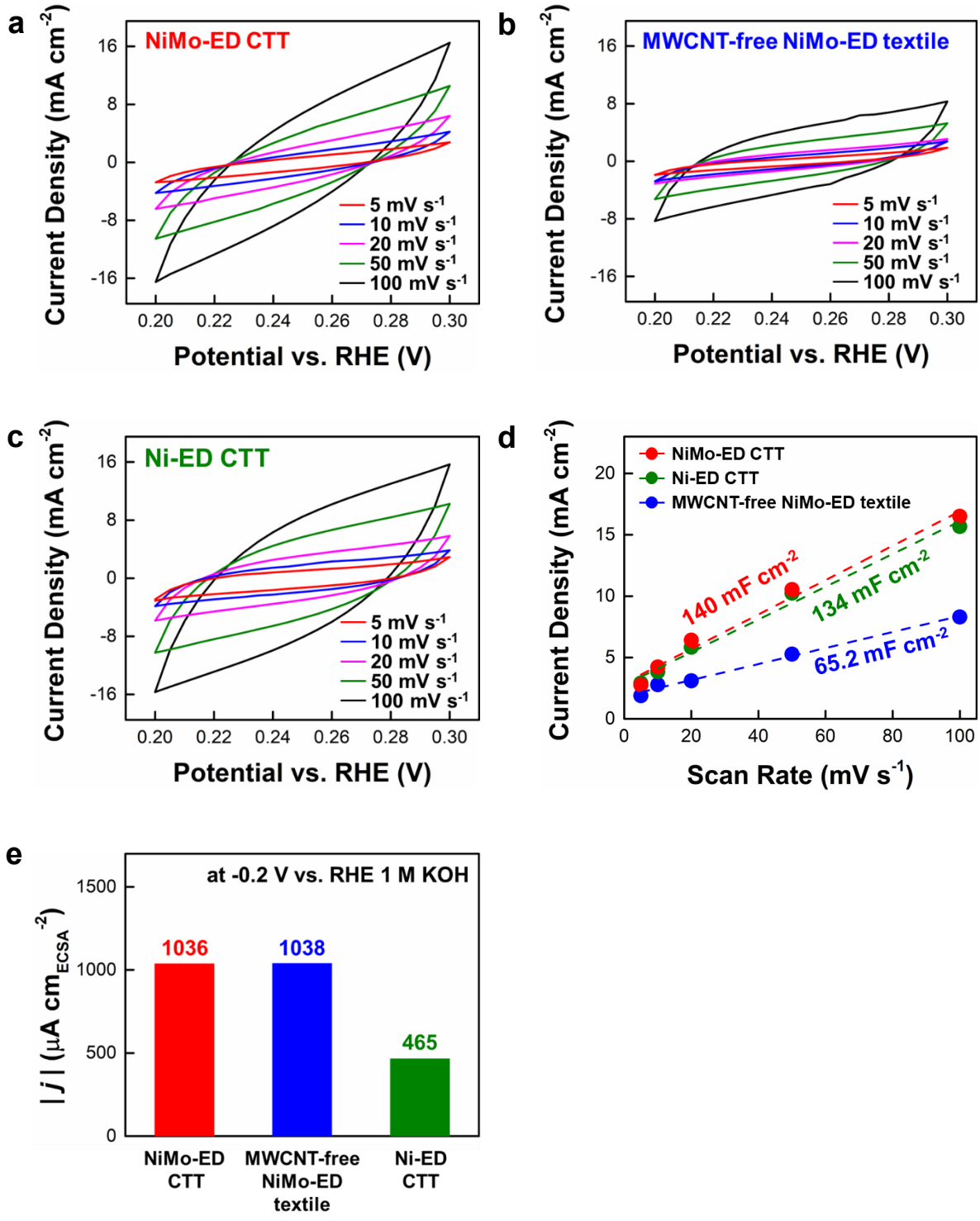

Fig. S15. ECSA data of HER electrodes. Scan rate-dependent CV curves of (a) NiMo–ED CTT, (b) MWCNT-free NiMo-ED textile, and (c) Ni-ED CTT in the non-faradaic region (0.2-0.3 V). (d) Double-layer capacitance (C_{dl}) for the electrodes calculated from linear fitting. (e) Normalized current densities ($|j|$) of three different HER electrodes with respect to the

corresponding ECSA values (876 cm^2 for NiMo–ED CTT, 834 cm^2 for Ni–ED CTT, and 407.5 cm^2 for MWCNT-free NiMo-ED textile calculated based on the specific capacitance of 40 μF cm^{-2} of Ni).

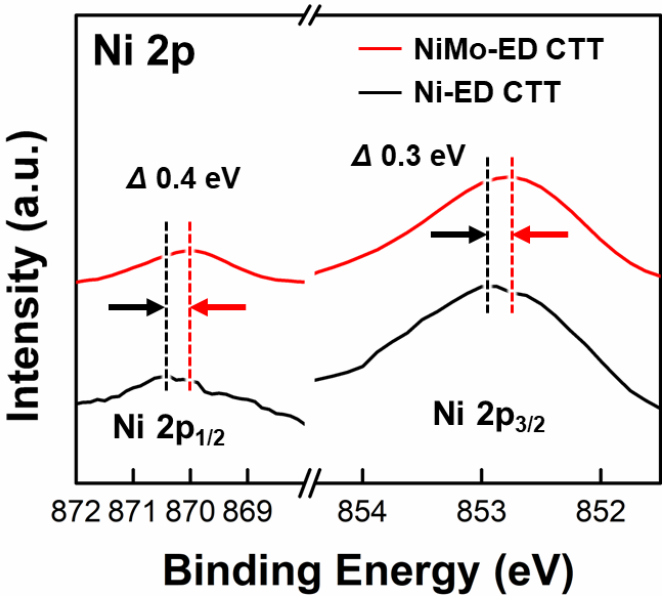

Fig. S16. Shift of Ni^0 peaks in XPS spectra. Ni^0 peaks in the core level Ni $2p_{1/2}$ and Ni $2p_{3/2}$ XPS spectra of NiMo–ED CTT and Ni-ED CTT.

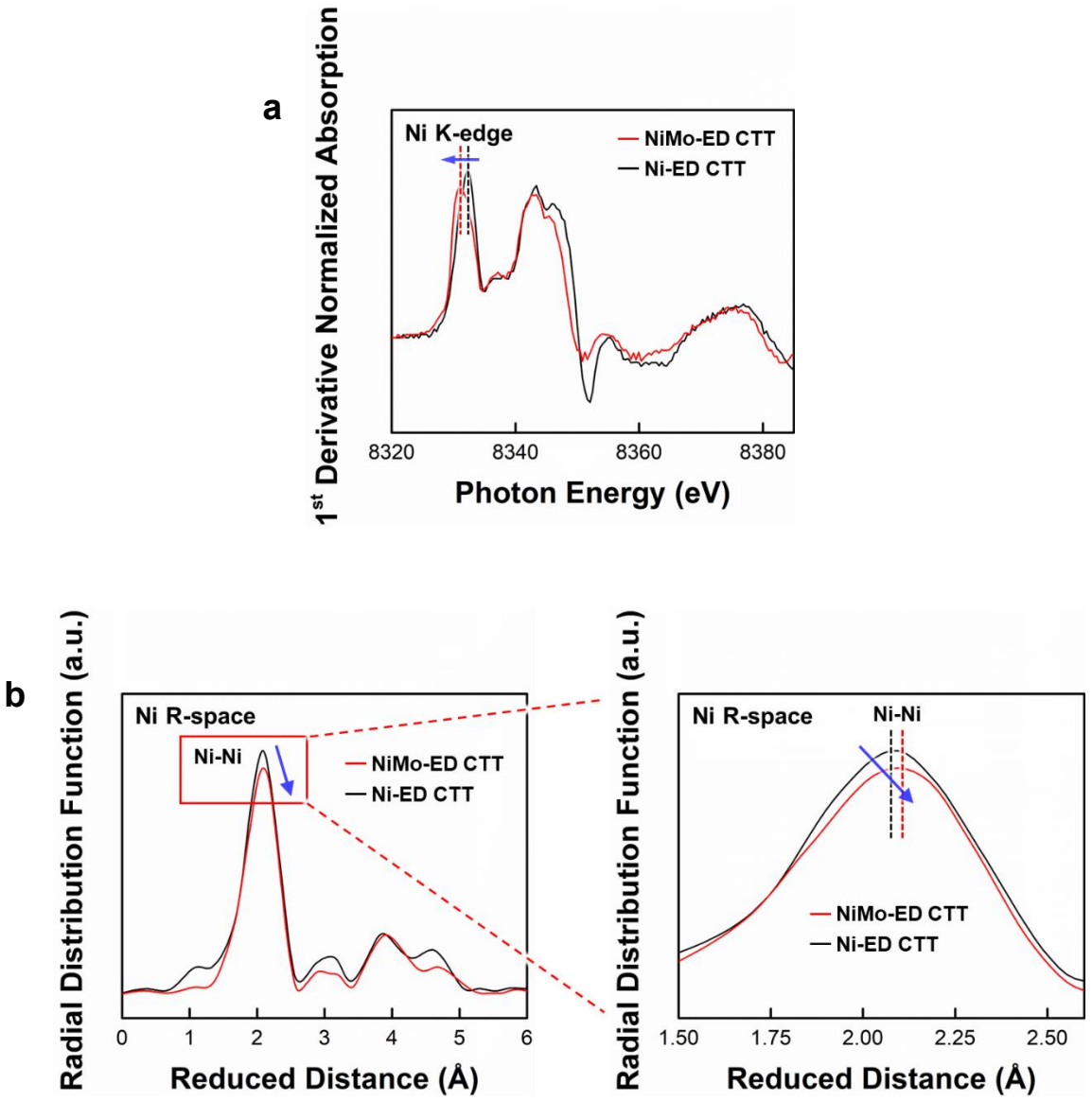

Fig. S17. Ni K-edge XAS characterization. (a) First derivatives of Ni K-edge XANES absorption edge and (b) EXAFS spectra for the NiMo-ED CTT and Ni-ED CTT. R indicates reduced distance.

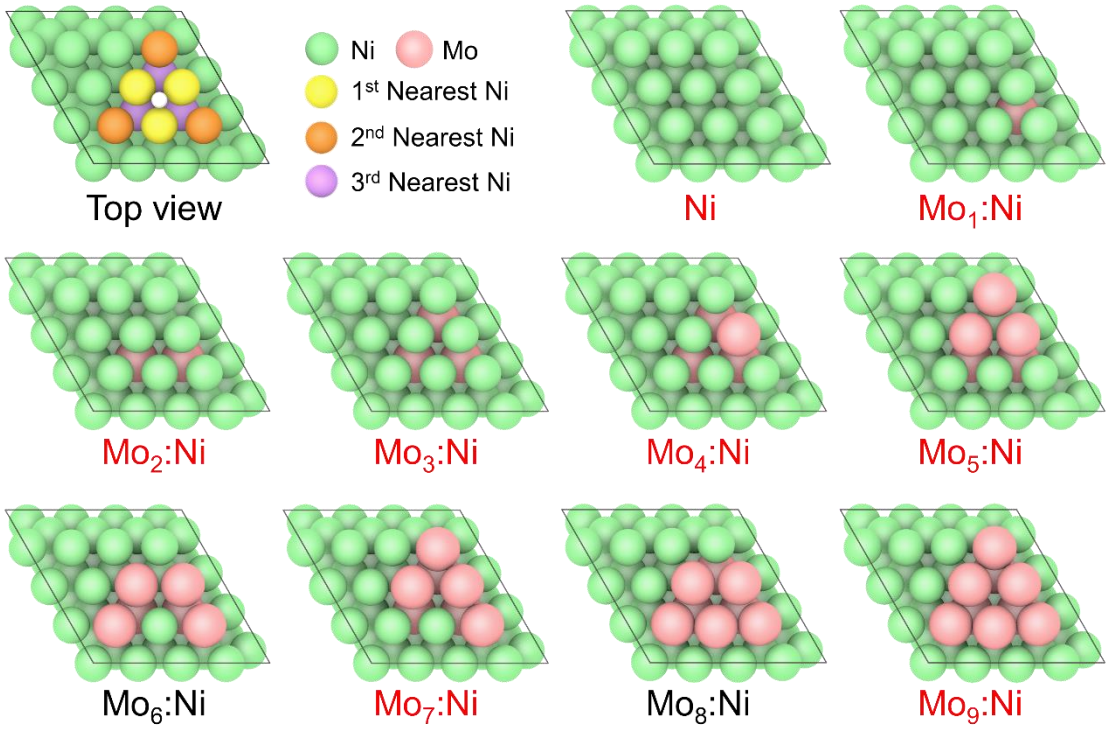

Fig. S18. Ni (111) and NiMo (111) model structures. Atomic configurations of the most stable surface for each number of substituted Mo atoms. The structures with the red color in the model name are convex hull points.

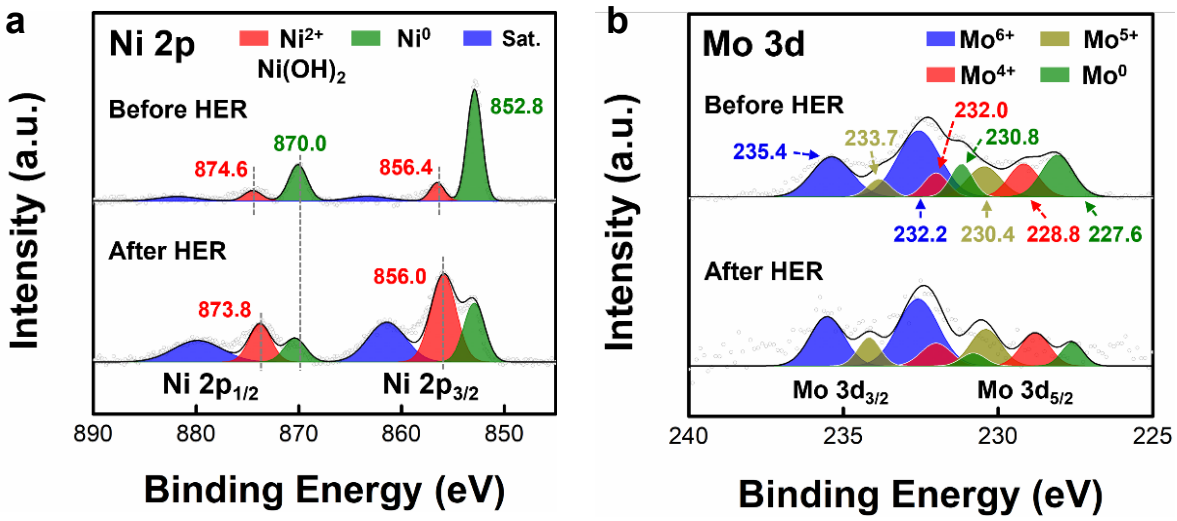

Fig. S19. XPS analysis. (a) Ni 2p, (b) Mo 3d XPS spectra of NiMo–ED CTT before and after HER stability test for 30 h.

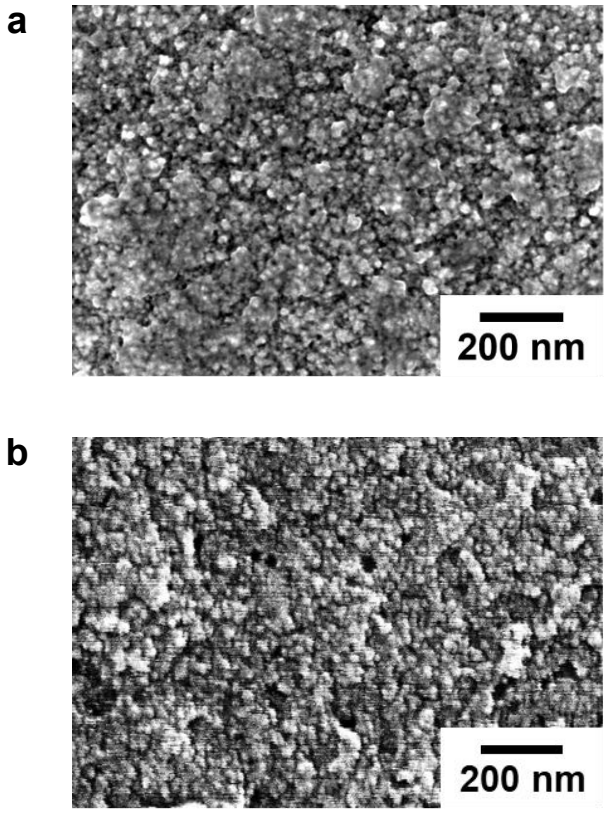

Fig. S20. FE-SEM images. Planar FE-SEM images of NiMo–ED CTT (a) before and (b) after the HER stability test for 30 h.

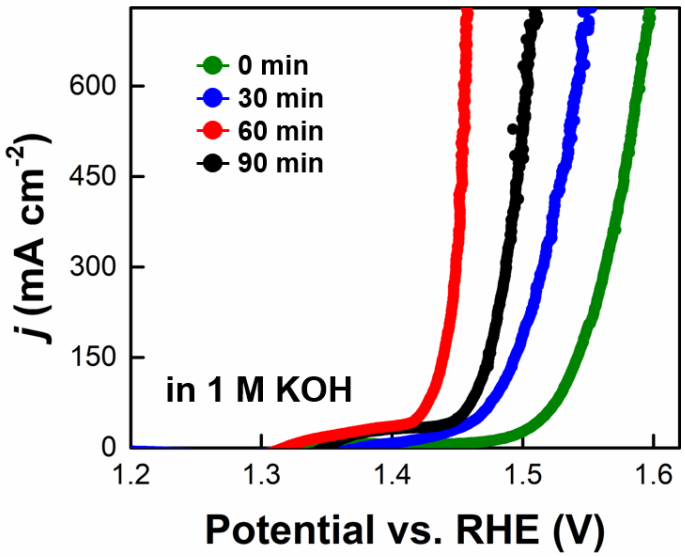

Fig. S21. OER polarization curves. The OER polarization curves of the NiFe-ED CTT with different electrodeposition time.

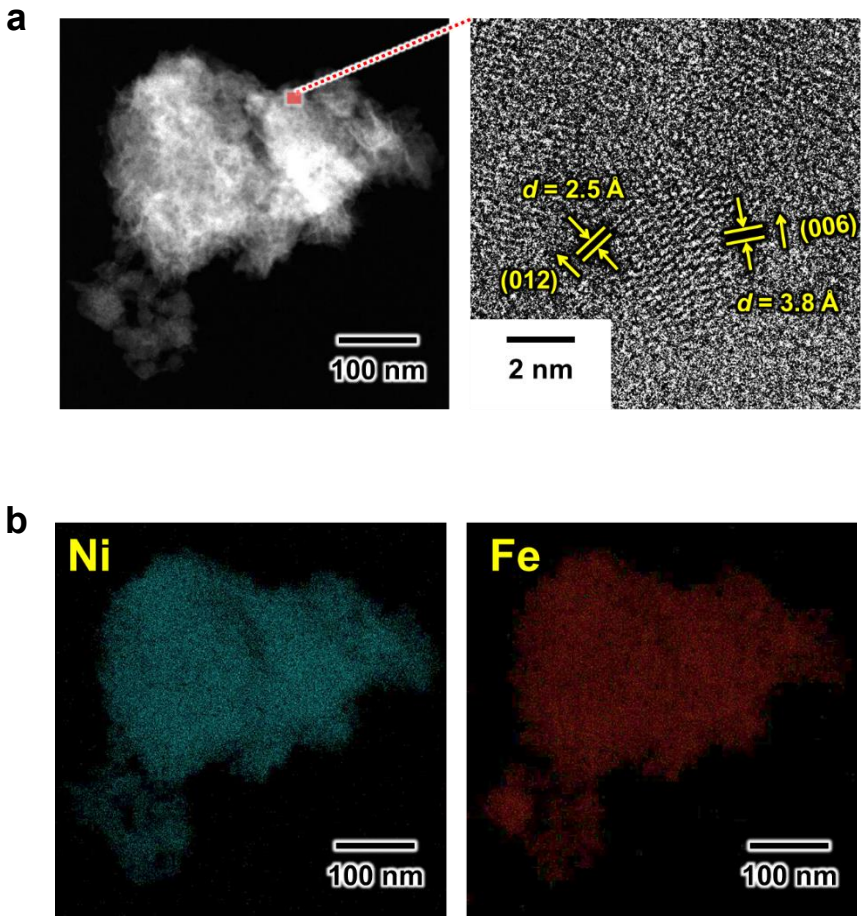

Fig. S22. HR-TEM analysis. (a) HR-TEM images and (b) its corresponding EDS mapping of NiFe-ED CTT.

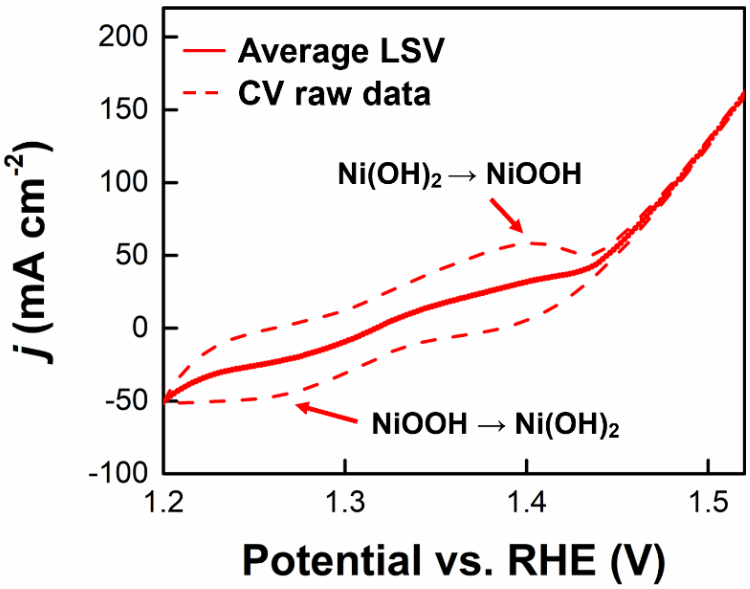

Fig. S23. Current densities of electrodes as a function of potential. CV curves of NiFe-ED CTT were recorded (dashed line). In a forward sweeps, NiFe-ED CTT showed peaks at potential of 1.4 V, which indicated the conversion of Ni(II) to Ni(III) (*i.e.*, conversion from $Ni(OH)_2$ to NiOOH). To alleviate this capacitive current, the OER polarization curve was obtained by averaging the current densities of forward and backward sweeps (solid line).

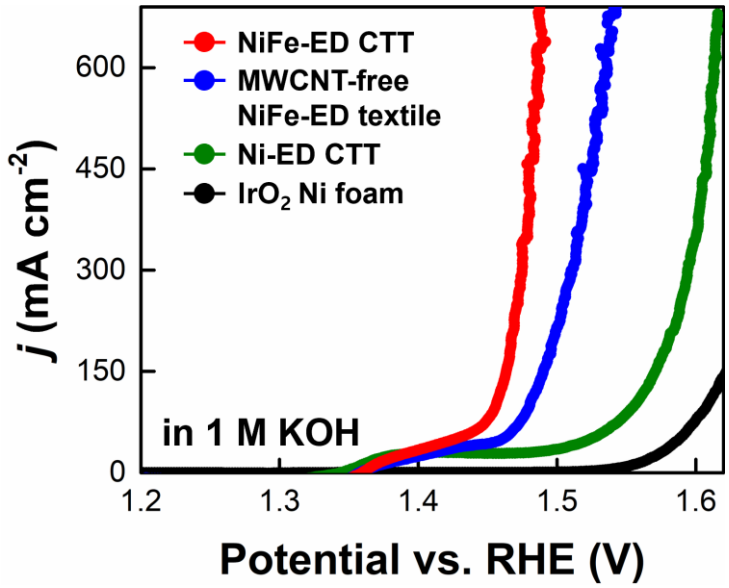

Fig. S24. OER polarization curves. The OER polarization curves of the NiFe-ED CTT, MWCNT-free NiFe-ED textile, Ni-ED CTT, and IrO_2 Ni foam measured using a graphite rod as a counter electrode.

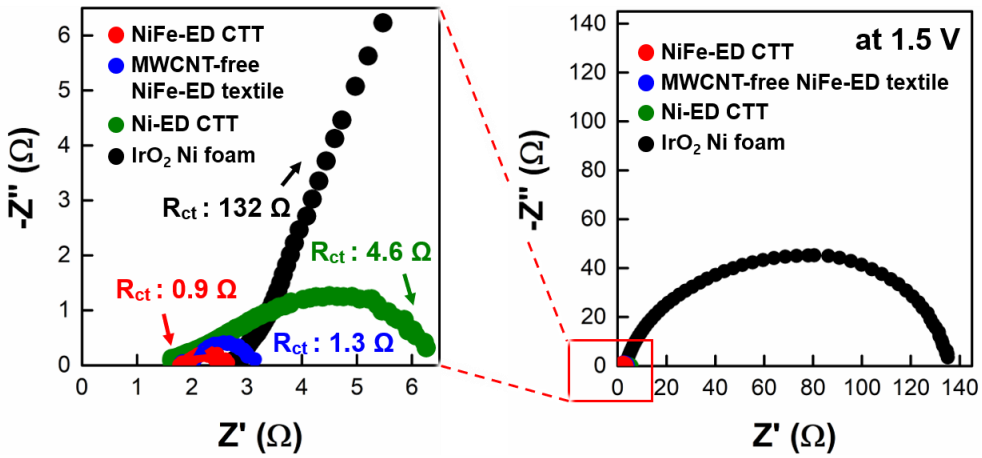

Fig. S25. EIS plots. EIS plots for the for NiFe-ED CTT, MWCNT-free NiFe-ED textile, Ni-ED CTT, and IrO_2 Ni foam at an applied potential of −1.5 V (*vs*. RHE).

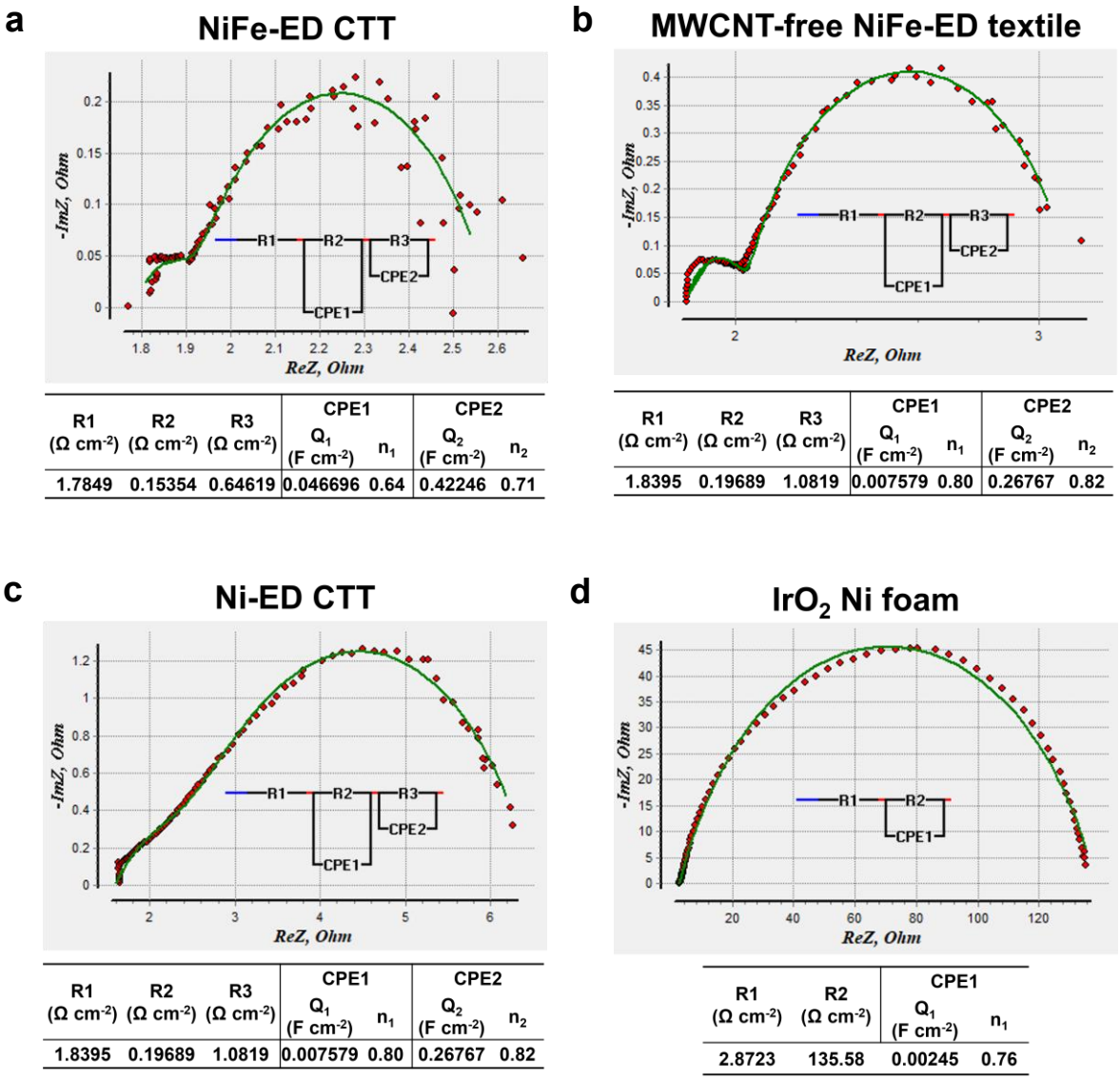

R1 (Ω cm^{-2})	R2 (Ω cm^{-2})	R3 (Ω cm^{-2})	CPE1 Q_1 (F cm^{-2})	CPE1 n_1	CPE2 Q_2 (F cm^{-2})	CPE2 n_2
1.7849	0.15354	0.64619	0.046696	0.64	0.42246	0.71

R1 (Ω cm^{-2})	R2 (Ω cm^{-2})	R3 (Ω cm^{-2})	CPE1 Q_1 (F cm^{-2})	CPE1 n_1	CPE2 Q_2 (F cm^{-2})	CPE2 n_2
1.8395	0.19689	1.0819	0.007579	0.80	0.26767	0.82

R1 (Ω cm^{-2})	R2 (Ω cm^{-2})	R3 (Ω cm^{-2})	CPE1 Q_1 (F cm^{-2})	CPE1 n_1	CPE2 Q_2 (F cm^{-2})	CPE2 n_2
1.8395	0.19689	1.0819	0.007579	0.80	0.26767	0.82

R1 (Ω cm^{-2})	R2 (Ω cm^{-2})	CPE1 Q_1 (F cm^{-2})	CPE1 n_1
2.8723	135.58	0.00245	0.76

Fig. S26. EIS plots of OER electrodes. EIS plots of (a) NiFe–ED CTT, (b) MWCNT-free NiFe-ED textile, (c) Ni-ED CTT, and (d) IrO_2-Ni foam with the corresponding equivalent circuit (inset).

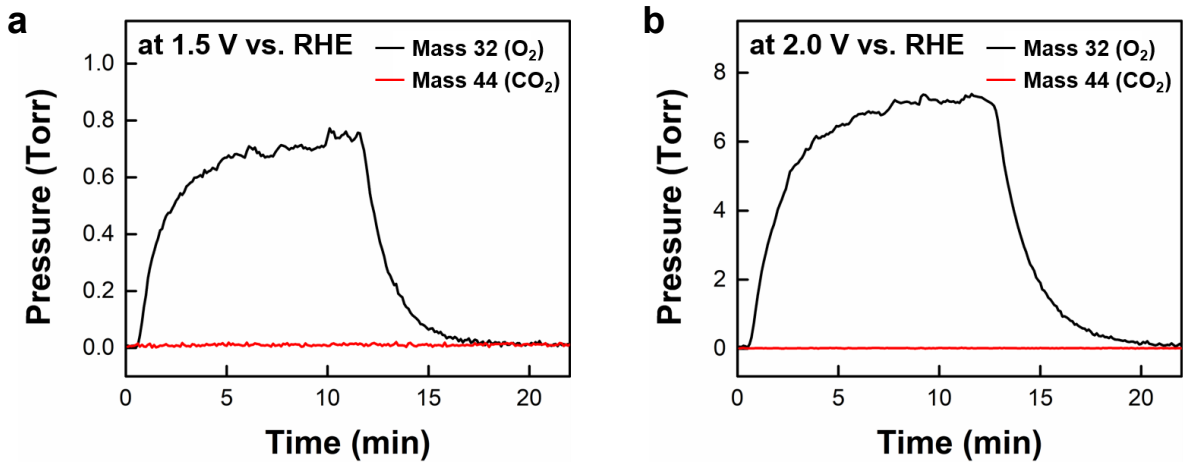

Fig. S27. Mass spectra of CO_2 and O_2 from the OER electrode. The mass spectra of CO_2 and O_2 from the OER electrode was examined to analyze carbon corrosion. This analysis was performed at voltage levels of (a) 1.5 V and (b) 2.0 V (vs. RHE). To assess carbon corrosion, a corrosion test was executed, involving the application of a consistent potential of 1.5 V and 2.0 V (vs. RHE) to the OER electrode for a duration of 10 min. The quantity of CO_2 released during this corrosion test, serving as a direct indicator of carbon corrosion, was measured over time using mass spectrometry. No traces of CO_2 gas were detected during the corrosion test, and this outcome strongly suggests the absence of carbon corrosion.

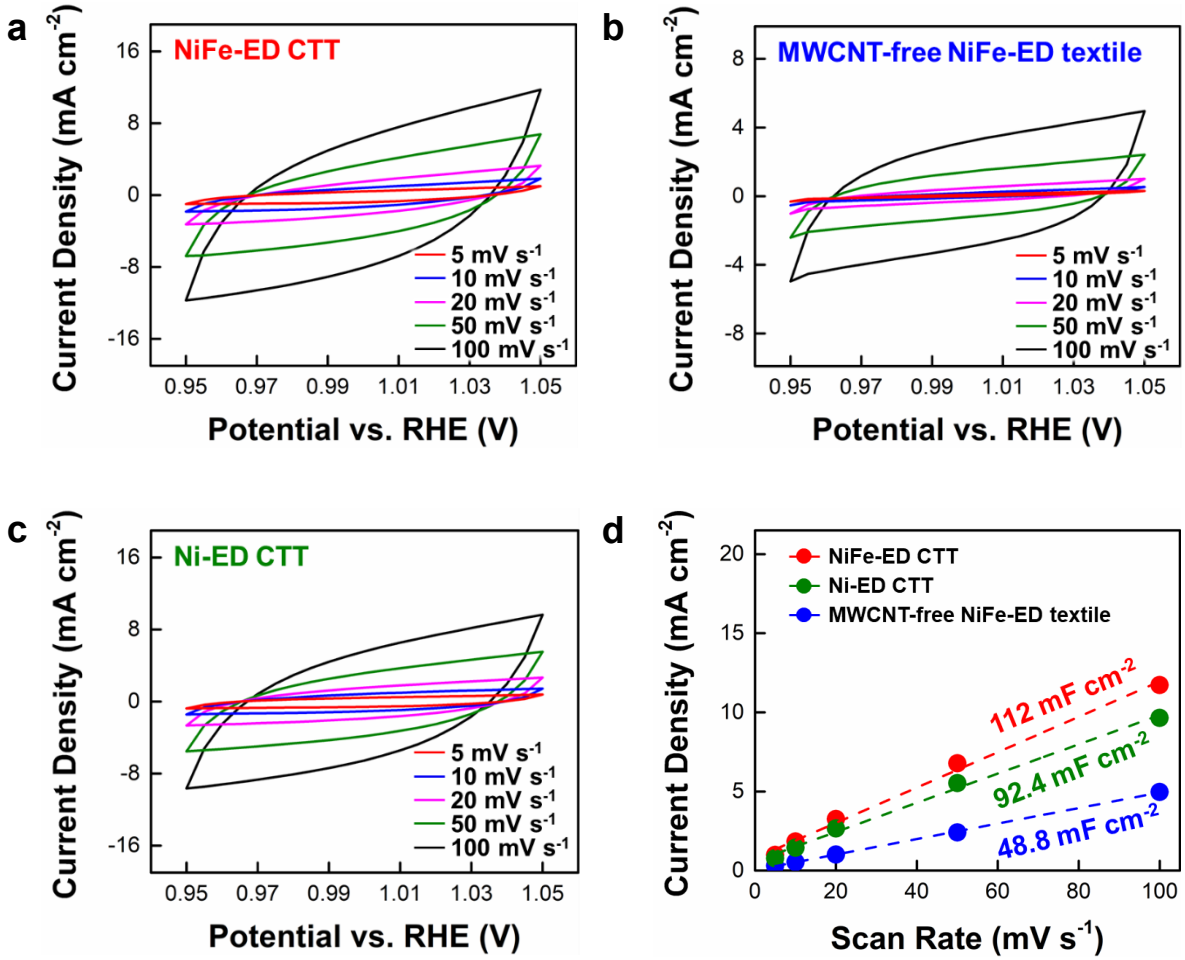

Fig. S28. ECSA data of OER electrodes. Scan rate-dependent CV curves of (a) NiFe–ED CTT, (b) MWCNT-free NiFe-ED textile, and (c) Ni-ED CTT in the non-faradaic region (0.95 - 1.05 V). (d) Double-layer capacitance (C_{dl}) for three different electrodes. As a result, ECSA values were calculated to be 698 cm^2 for NiFe–ED CTT, 577 cm^2 for Ni–ED CTT, and 306 cm^2 for MWCNT-free NiFe-ED textile based on the specific capacitance of 40 μF cm^{-2} of Ni).

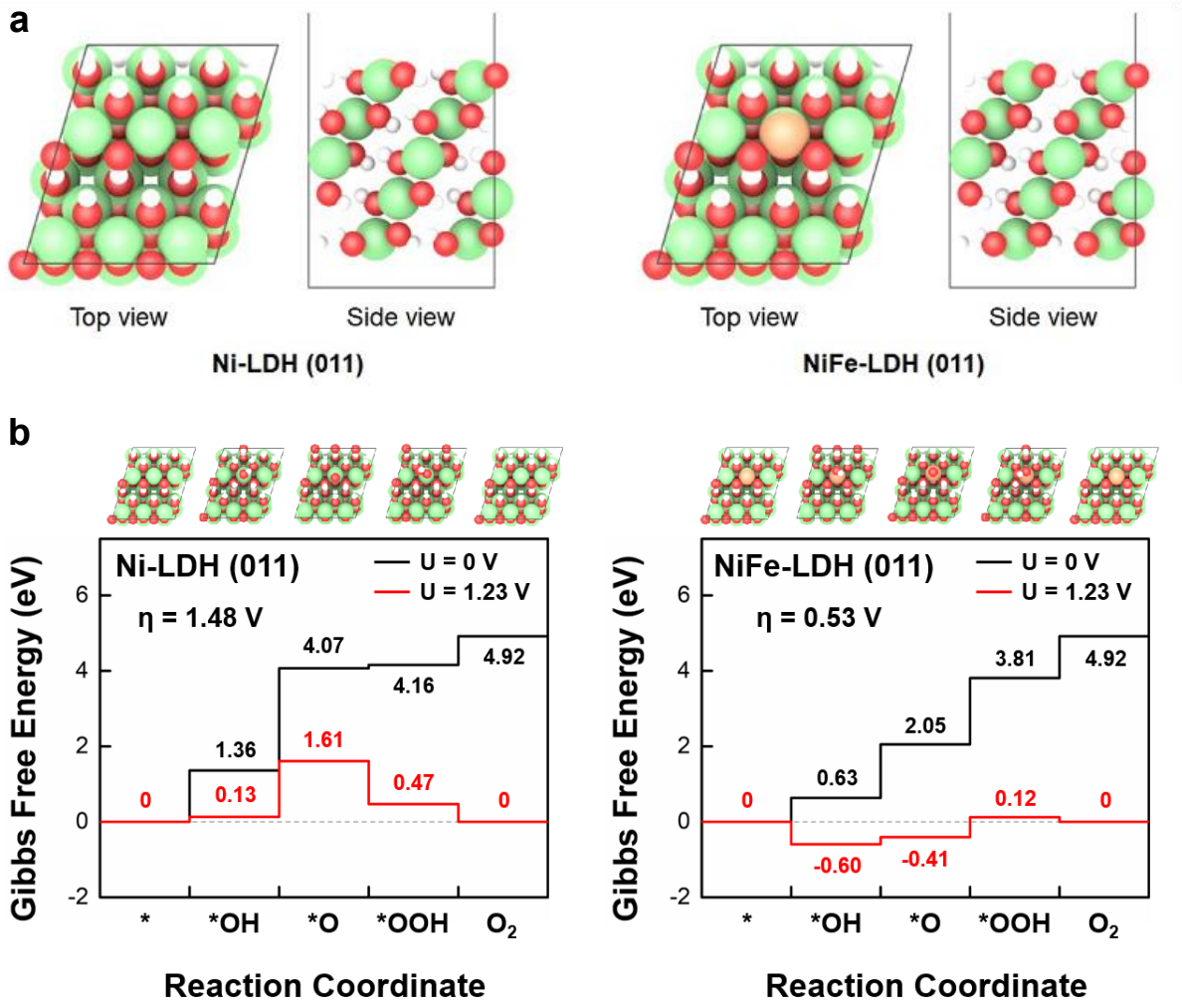

Fig. S29. OER DFT calculation. (a) Geometry-optimized atomic structures of Ni- and NiFe-LDH structures. (b) the Gibbs free energy diagram of OER for Ni- and NiFe-LDH.

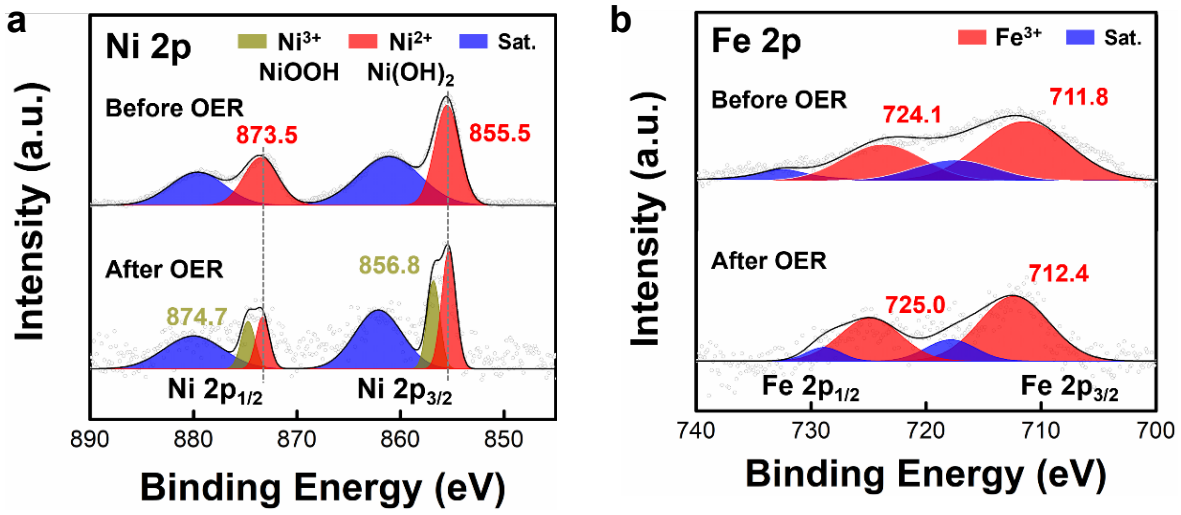

Fig. S30. XPS analysis. (a) Ni 2p, (b) Fe 2p XPS spectra of NiFe–ED CTT before and after OER stability test for 30 h.

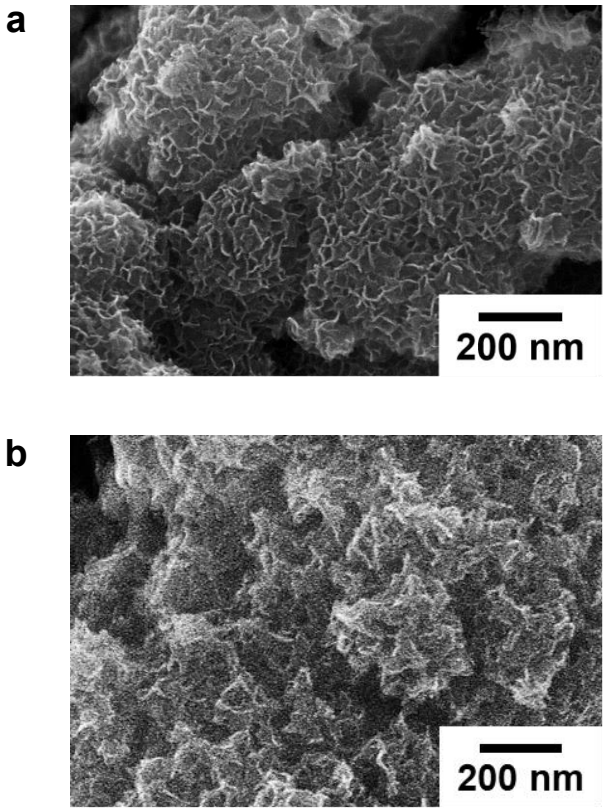

Fig. S31. FE-SEM images. Planar FE-SEM images of NiFe–ED CTT (a) before and (b) after the OER stability test for 30 h.

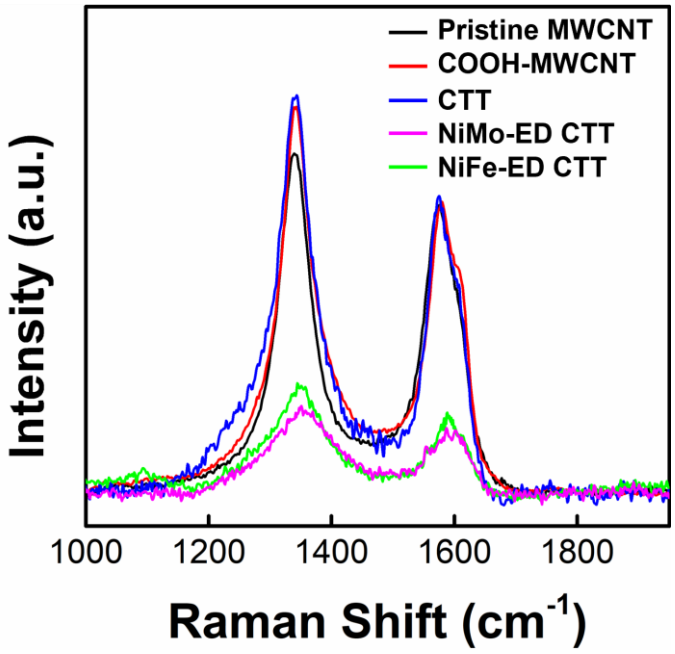

Fig. S32. Raman spectra. The raman spectra of the pristine MWCNT, COOH-MWCNT, CTT, NiMo-ED CTT, and NiFe-ED CTT.

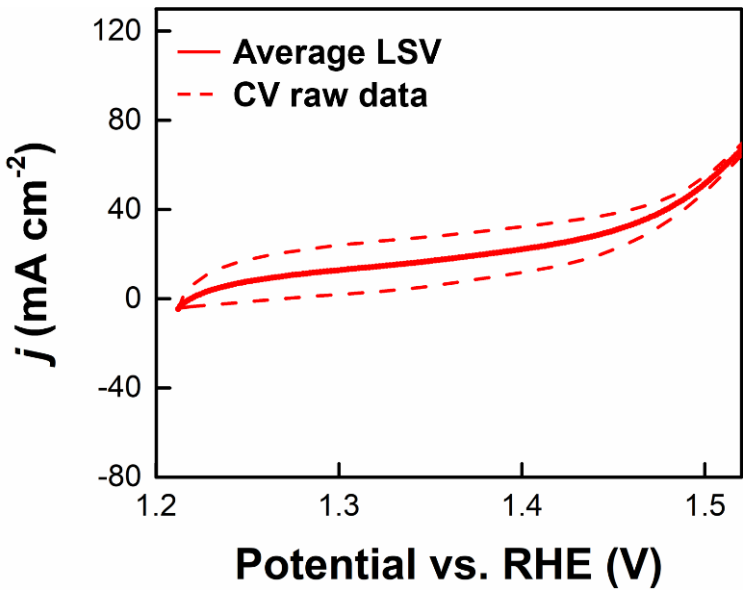

Fig. S33. Current densities of electrodes as a function of potential. CV curves of NiMo–ED CTT cathode‖NiFe–ED CTT anode were recorded (dashed line). The difference between a forward and reverse sweeps was attributed to capacitive current and Ni oxidation current. The polarization curves of water-splitting devices were derived by averaging the measured values obtained from both forward and reverse sweeps of the CV curves (solid line). This averaging process aimed to reduce the impact of capacitive current and Ni oxidation current on the results.

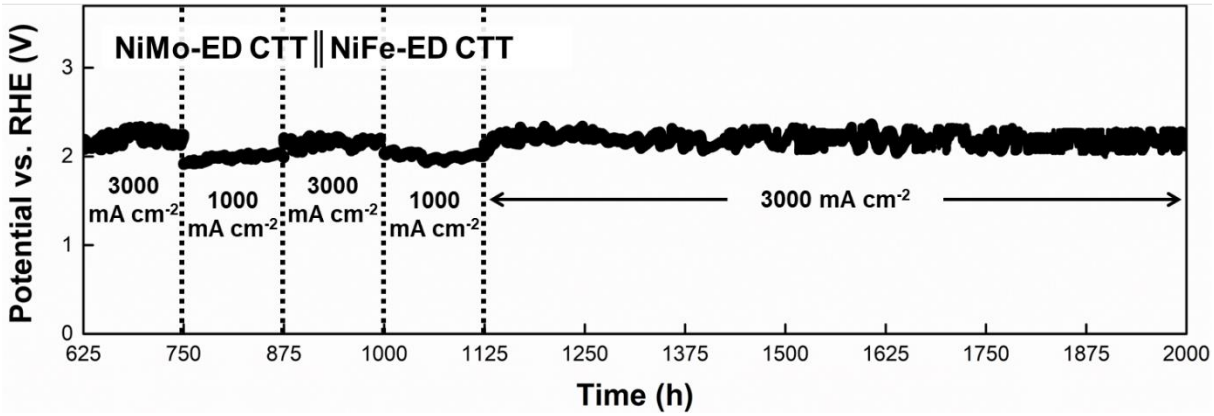

Fig. S34. Stability test. Chronopotentiometry curve of NiMo-ED CTT‖NiFe-ED CTT cell at at variable current densities of 3,000 mA cm^{-2} and 1,000 mA cm^{-2}, alternately.

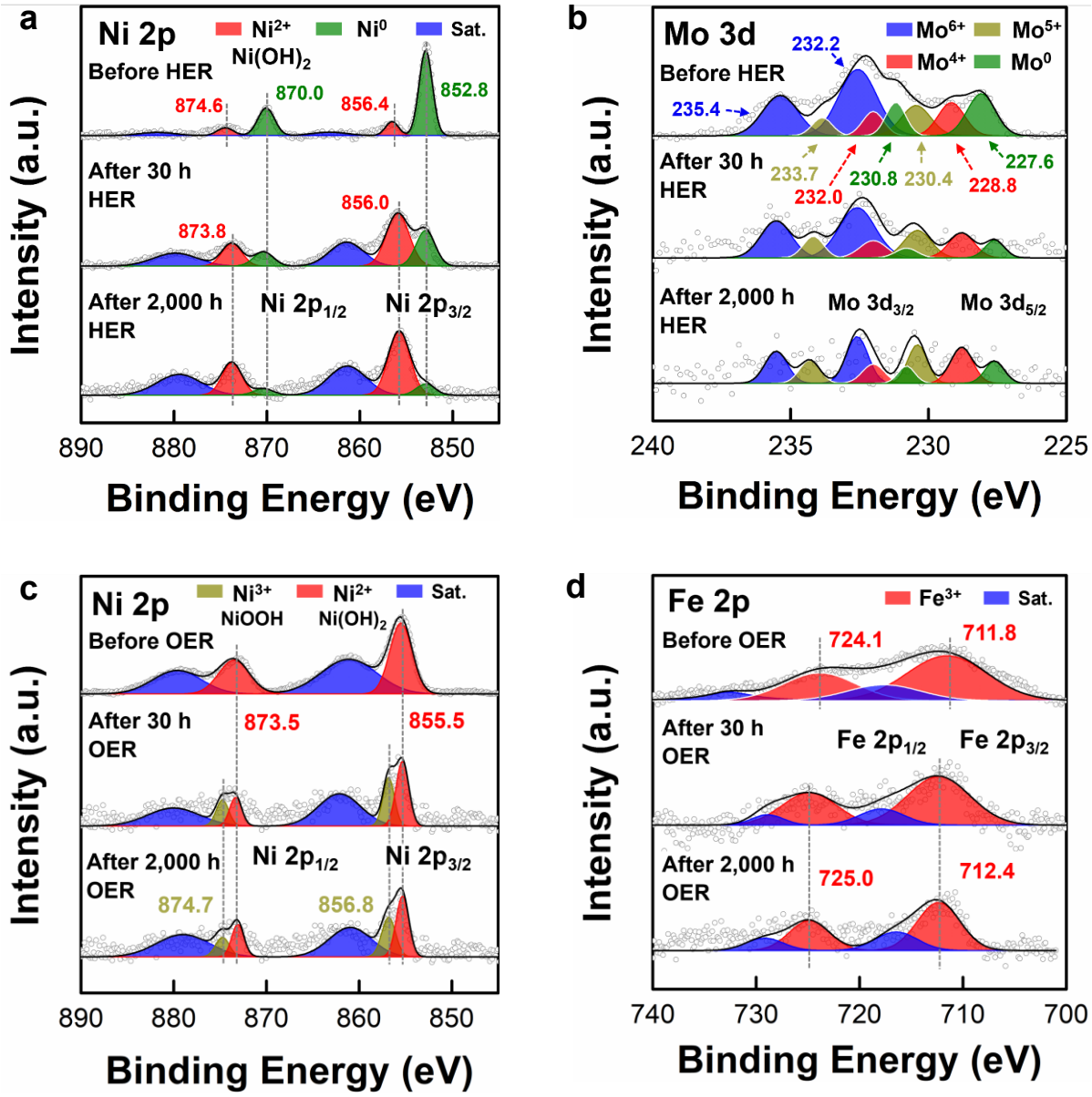

Fig. S35. XPS analysis. (a) Ni 2p, (b) Mo 3d XPS spectra of NiMo–ED CTT and (c) Ni 2p, (d) Fe 2p XPS spectra of NiFe–ED CTT before and after stability test for 30 h (half-cell) and 2,000 h (full-cell).

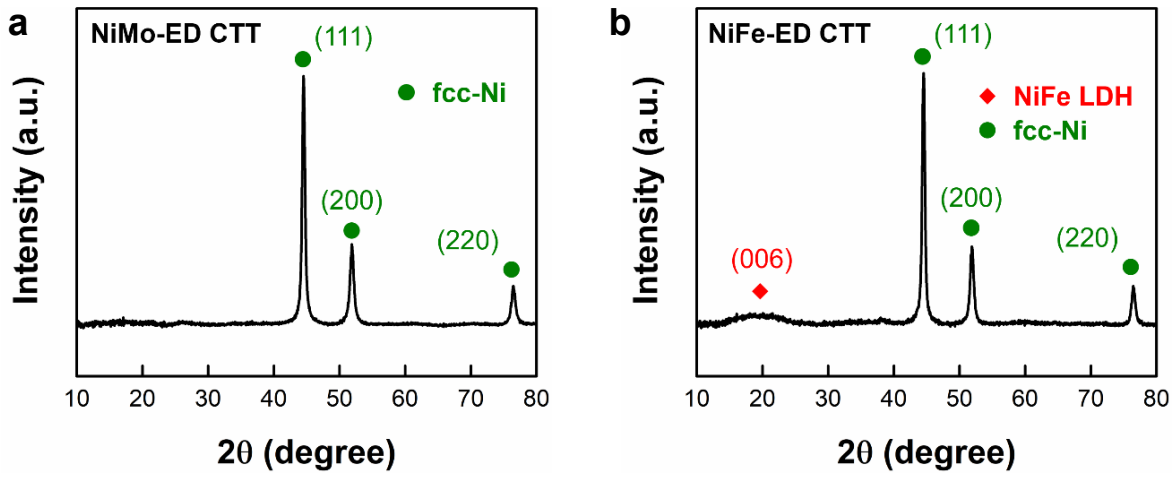

Fig. S36. XRD analysis. XRD patterns of (a) NiMo–ED CTT and (b) NiFe-ED CTT after stability test for 2,000 h.

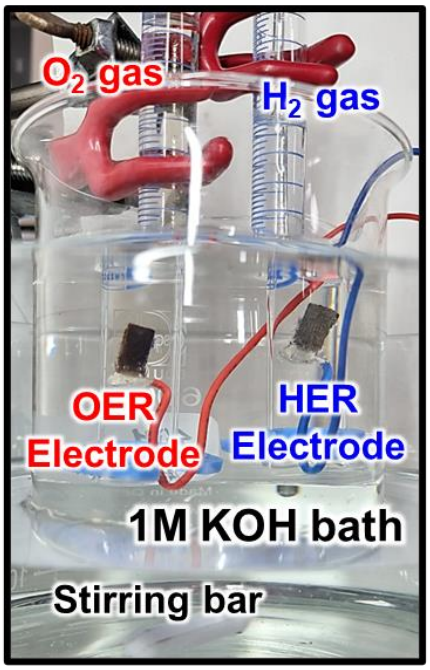

Fig. S37. Photographic image. The photographic image of full-cell water-splitting device composed of the NiMo-ED CTT‖NiFe-ED CTT electrodes. Hydrogen and oxygen gases are generated and collected in the cylinders.

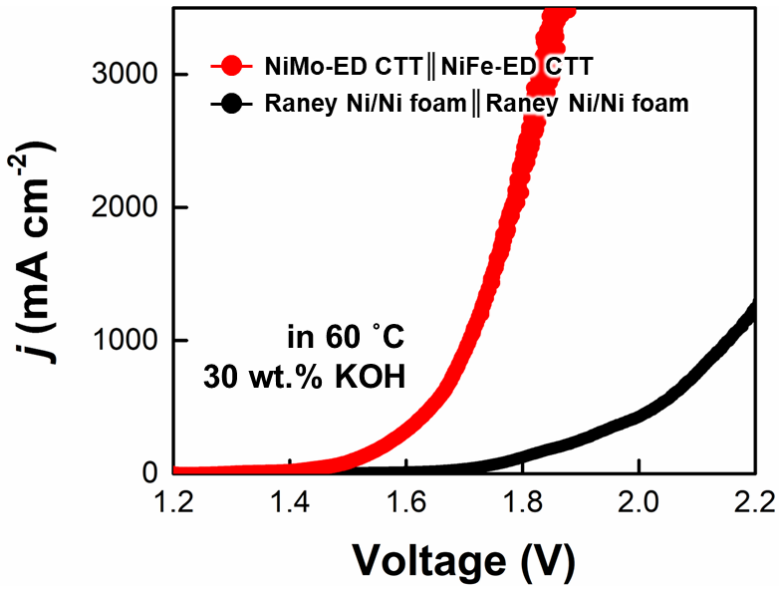

Fig. S38. Polarization curves. Polarization curves of NiMo-ED CTT‖NiFe-ED CTT and conventional water-splitting electrodes (Raney nickel/Ni foam) measured in a 30 wt.% KOH electrolyte at 60 ℃.

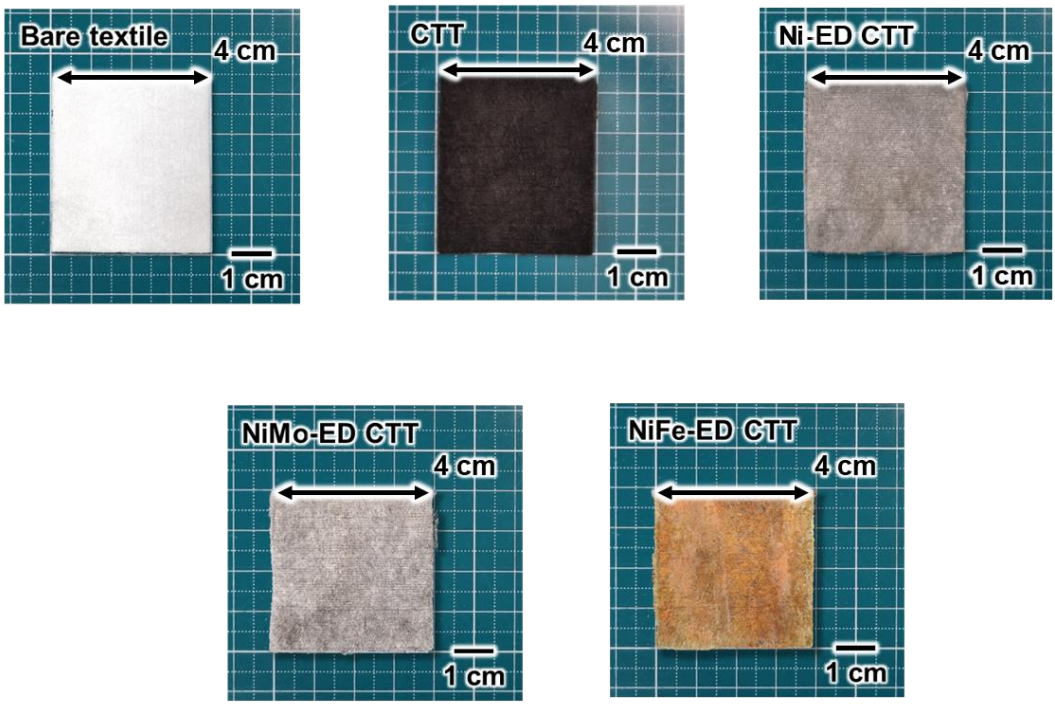

Fig. S39. Photographic images. Photographic images of bare textile, CTT, Ni-ED CTT, NiMo-ED CTT, and NiFe-ED CTT.

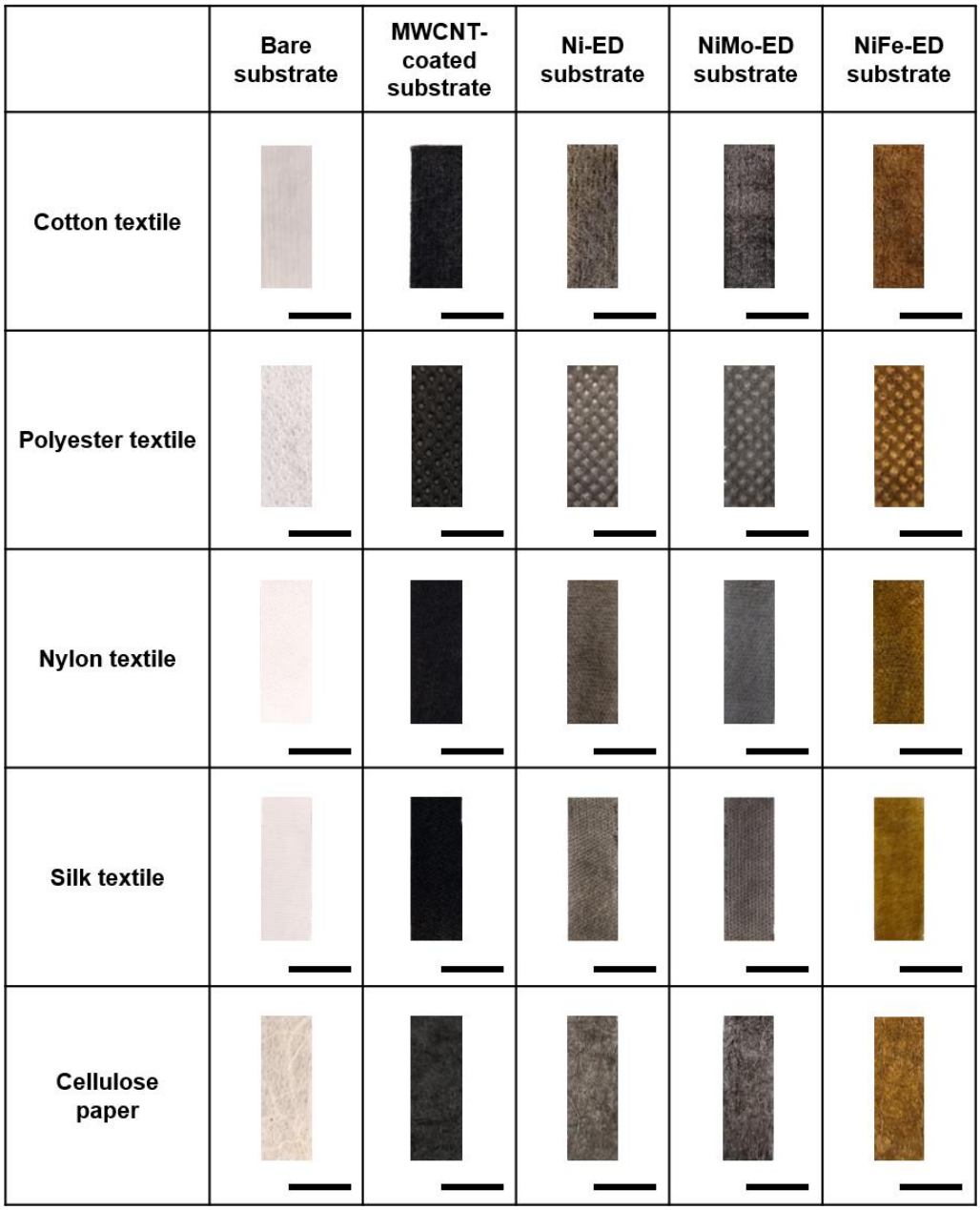

Fig. S40. **Photographic images.** Photographic images of electrodes based on cotton, polyester, nylon, and silk textile and cellulose paper. (scale bar, 0.5 cm)

Table S1. HER overpotentials (η) at 10, 1,000, and 3,000 mA cm^{-2} and resistance values for NiMo-ED CTT, MWCNT-free NiMo-ED textile, Ni-ED CTT, and Pt/C Ni foam.

	η_{10} (mV)	$\eta_{1,000}$ (mV)	$\eta_{3,000}$ (mV)	R_s (Ω)	R_{ct} (Ω)
NiMo-ED CTT	8	203	233	1.5	1.8
MWCNT-free NiMo-ED textile	20	251	348	1.5	3.7
Ni-ED CTT	15	305	401	1.6	4.6
Pt/C Ni foam	19	520	-	3.1	6.1

Table S2. OER overpotentials (η) at 50, 100, 1,000, and 3,000 mA cm^{-2} and resistance values for NiFe-ED CTT, MWCNT-free NiFe-ED textile, Ni-ED CTT, and IrO_2 Ni foam.

	η_{50} (mV)	η_{100} (mV)	$\eta_{1,000}$ (mV)	$\eta_{3,000}$ (mV)	R_s (Ω)	R_{ct} (Ω)
NiFe-ED CTT	189	202	227	250	1.8	0.9
MWCNT-free NiFe-ED textile	227	241	307	444	1.8	1.3
Ni-ED CTT	285	301	384	522	1.5	11.8
IrO_2 Ni foam	316	334	497	-	2.8	132

Table S3. Cell voltages at 10, 100, 1,000, and 3,000 mA cm^{-2} of NiMo-ED CTT‖NiFe-ED CTT, MWCNT-free NiMo–ED textile‖ MWCNT-free NiFe–ED textile, symmetric Ni-ED CTT‖Ni-ED CTT, and conventional water-splitting electrodes (Pt/C Ni foam‖IrO_2 Ni foam).

	Cell voltage (V)			
	10 mA cm^{-2}	**100 mA cm^{-2}**	**1,000 mA cm^{-2}**	**3,000 mA cm^{-2}**
NiMo-ED CTT‖ NiFe-ED CTT	1.34	1.55	1.77	2.01
MWCNT-free NiMo-ED textile‖ NiFe-ED textile	1.47	1.62	1.92	2.35
Ni-ED CTT‖ Ni-ED CTT	1.40	1.71	1.99	-
Pt/C Ni foam‖ IrO_2 Ni foam	1.56	1.72	2.04	-

Table S4. ICP-MS data. ICP-MS data of electrolyte (KOH) after 20 h of water splitting reaction at current density of 3,000 mA cm^{-2}.

	ICP-MS data of KOH after 20 hours of test
Ni	Not detected (< 111.1 μg/L)
Mo	Not detected (< 111.1 μg/L)
Fe	3 μg/L

* Fe contents were calculated by subtracting the value of the unrreacted solution from the value of the reacted solution.

Table S5. Performance comparison of Ni-based HER electrodes.

HER catalyst	Method	Overpotential (mV)	Tafel plot (mV dec^{-1})	Reference
NiMo-ED CTT	**MWCNT assembly induced electrodeposition**	**8 @10 mA cm^{-2}**	**28.5**	**Our work**
$(Ni_xFe_yCo_{6-x-y})$ Mo_6C/Ni Foam	Hydrothermal	20 @10 mA cm^{-2}	55.1	[S15]
$NiMoO_4$-H_2/ Ni Foam	Hydrothermal	21 @10 mA cm^{-2}	-	[S16]
Ni/$NiFeMoO_x$/ Ni foam	Hydrothermal	22 @10 mA cm^{-2}	76	[S17]
NiMo/Ni-P Cellulose paper	Electrodeposition, electroless plating	32 @10 mA cm^{-2}	60.9	[S18]
Ni-MoO_2/ Ni foam	Induction heating	39 @10 mA cm^{-2}	75.0	[S19]
NiFeMo/ Ni foam	Hydrothermal	45 @10 mA cm^{-2}	-	[S20]
Ni_5Co_3Mo-OH nanosheets/Ni foam	Chloride corrosion	52 @10 mA cm^{-2}	59	[S21]
NiFeOx@NiCu	Solvothermal	66 @10 mA cm^{-2}	67.8	[S22]
FeNi-MOF/ Ni foam	Solvothermal	79 @10 mA cm^{-2}	30.1	[S23]
N-Ni_3S_2/Ni foam	Thiourea calcination	110 @10 mA cm^{-2}	-	[S24]
NiMo-PVP/ Carbon cloth	Dip coating, annealing	130 @10 mA cm^{-2}	84	[S25]

Table S6. Performance comparison of Ni-based OER electrodes

OER catalyst	Method	Overpotential (mV)	Tafel plot (mV dec^{-1})	Reference
NiFe-ED CTT	**MWCNT assembly induced electrodeposition**	**103 @10 mA cm^{-2} 189 @50 mA cm^{-2} 202 @100 mA cm^{-2}**	**30.1**	**Our work**
Ni–Fe LDH@NiCu	Solvothermal	218 @10 mA cm^{-2}	56.9	[S22]
NiFeMo/ Ni foam	Hydrothermal	238 @10 mA cm^{-2}	35	[S20]
NiFe LDH/ Ni foam	Induction heating	246 @10 mA cm^{-2}	46.6	[S19]
NiFe-PVP/ Carbon cloth	Dip coating, annealing	297 @10 mA cm^{-2}	48	[S25]
FeNi-MOF/ Ni foam	Solvothermal	235 @50 mA cm^{-2}	55.4	[S23]
NiFe/Ni-P Cellulose paper	Electrodeposition, electroless plating	240 @50 mA cm^{-2}	29.7	[S18]
Ni_xFeN/Ni_3N/ Ni Foam	Thermal nitridation	258 @100 mA cm^{-2}	43	[S16]
$Ni/NiFeMoO_x$/ Ni foam	Hydrothermal	289 @100 mA cm^{-2}	35	[S17]
Ni_5Co_3Mo-OH nanosheets/Ni foam	Chloride corrosion	304 @100 mA cm^{-2}	56.4	[S21]

Table S7. Performance comparison of Ni-based overall water splitting electrodes

HER catalyst (Cathode)	OER catalyst (Anode)	Voltage (V)	Current density (mA cm^{-2})	Durability (hour)	Reference
NiMo-ED CTT	**NiFe-ED CTT**	**1.34 @10 mA cm^{-2} 1.55 @100 mA cm^{-2} 1.77 @1,000 mA cm^{-2} 2.01 @3,000 mA cm^{-2}**	**3,000**	**1,000**	**Our work**
FeP/Ni_2P/Ni foam	FeP/Ni_2P/Ni foam	1.42 @10 mA cm^{-2} 1.60 @100 mA cm^{-2} 1.72 @500 mA cm^{-2} 1.78 @1,000 mA cm^{-2}	500	40	[S26]
Ni_5Co_3Mo-OH nanosheets/Ni foam	Ni_5Co_3Mo-OH nanosheets/Ni foam	1.43 @10 mA cm^{-2} 1.60 @100 mA cm^{-2}	100	100	[S21]
Ni_2P Ni Foam	NiFe LDH Ni Foam	1.60 @43 mA cm^{-2} 2.00 @860 mA cm^{-2}	1,250	16	[S27]
Ni–P–B paper	Ni–P–B paper	1.44 @10 mA cm^{-2} 1.66 @50 mA cm^{-2} 1.79 @200 mA cm^{-2}	1,000	60	[S28]
NiMo/Ni-P Cellulose paper	NiFe/Ni-P Cellulose paper	1.51 @10 mA cm^{-2} 1.75 @40 mA cm^{-2}	15	200	[S18]
Ni-MoO_2/ Ni foam	NiFe LDH/ Ni foam	1.50 @10 mA cm^{-2} 2.00 @200 mA cm^{-2}	25	12	[S19]

MnOx/NiFeP Ni Foam	MnOx/NiFeP Ni Foam	1.69 @100 mA cm^{-2} 1.83 @1,000 mA cm^{-2}	500	120	[S29]
NiFeMo/ Ni foam	NiFeMo/ Ni foam	1.45 @10 mA cm^{-2}	50	50	[S20]
Ni-Mo-P aerogel	Ni-Mo-P aerogel	1.46 @10 mA cm^{-2}	10	40	[S30]
$(Ni_xFe_yCo_{6-x-y})$ Mo_6C/Ni Foam	$(Ni_xFe_yCo_{6-x-y})$ Mo_6C/Ni Foam	1.47 @10 mA cm^{-2}	500	50	[S15]
N-Ni_3S_2/Ni foam	N-Ni_3S_2/Ni foam	1.48 @10 mA cm^{-2}	20	8	[S24]
FeNi-MOF/ Ni foam	FeNi-MOF/ Ni foam	1.495 @10 mA cm^{-2}	500	100	[S23]
Ni/NiFeMoO_x/ Ni foam	Ni/NiFeMoO_x/ Ni foam	1.50 @10 mA cm^{-2}	500	100	[S17]
$Ni_{2(1-x)}Mo_{2x}P$/ Ni Foam	Cu@NiFe LDH /Ni Foam	1.51 @10 mA cm^{-2}	10-500	70	[S31]
NiFeOx@NiCu	Ni–Fe LDH@NiCu	1.52 @10 mA cm^{-2}	50	10	[S22]

Supplementary references

[S1] M. R. Deakin, D. A. Buttry, Electrochemical applications of the quartz crystal microbalance. Anal. Chem. Soc. 61 (1989) 1147A-1154A. https://doi.org/10.1021/ac00195a001

[S2] J. Yin, Y. Li, F. Lv, Q. Fan, Y-Q. Zhao, Q. Zhang, W. Wang, F. Cheng, P. Xi, S. Guo, NiO/CoN Porous Nanowires as Efficient Bifunctional Catalysts for Zn–Air Batteries. ACS Nano 11 (2017) 2275–2283. https://doi.org/10.1021/acsnano.7b00417.

[S3] G. Kresse, J. Hafner, Ab initio molecular dynamics for liquid metals. Phys. Rev. B 47 (1993) 558-561. https://doi.org/10.1103/PhysRevB.47.558.

[S4] G. Kresse, J. Hafner, Ab initio molecular-dynamics simulation of the liquid-metal-amorphous-semiconductor transition in germanium. Phys. Rev. B 49 (1994) 14251-14269. https://doi.org/10.1103/PhysRevB.49.14251.

[S5] G. Kresse, J. Furthmüller, Efficient iterative schemes for ab initio total-energy calculations using a plane-wave basis set. Phys. Rev. B 54 (1996) 11169-11186. https://doi.org/10.1103/PhysRevB.54.11169.

[S6] G. Kresse, J. Furthmüller, Efficiency of ab-initio total energy calculations for metals and semiconductors using a plane-wave basis set. Comput. Mater. Sci. 6 (1996) 15-50. https://doi.org/10.1016/0927-0256(96)00008-0.

[S7] J. P. Perdew, K. Burke, M. Ernzerhof, Generalized gradient approximation made simple. Phys. Rev. Lett. 77 (1996) 3865-3868. https://doi.org/10.1103/PhysRevLett.77.3865.

[S8] P. E. Blöchl, Projector augmented-wave method. Phys. Rev. B 50 (1994) 17953-17979. https://doi.org/10.1103/PhysRevB.50.17953.

[S9] G. Kresse, D. Joubert, From ultrasoft pseudopotentials to the projector augmented-wave method. Phys. Rev. B 59 (1999) 1758-1775. https://doi.org/10.1103/PhysRevB.59.1758.

[S10] H. J. Monkhorst, J. D. Pack, Special points for Brillouin-zone integrations. Phys. Rev. B 13 (1976) 5188-5192. https://doi.org/10.1103/PhysRevB.13.5188.

[S11] S. L. Dudarev, G. A. Botton, S. Y. Savrasov, C. J. Humphreys, A. P. Sutton, Electron-energy-loss spectra and the structural stability of nickel oxide: An LSDA+U study. Phys. Rev. B 57 (1988) 1505-1509. https://doi.org/10.1103/PhysRevB.57.1505.

[S12] M. Cococcioni, S. de Gironcoli, Linear response approach to the calculation of the effective interaction parameters in the LDA+U method. Phys. Rev. B 71 (2005) 035105. https://doi.org/10.1103/PhysRevB.71.035105.

[S13] S.-E. Jang, H. Kim, Effect of water electrolysis catalysts on carbon corrosion in polymer electrolyte membrane fuel cells, J. Am. Chem. Soc. 132 (2010) 14700–14701. https://doi.org/10.1021/ja104672n.

[S14] S. Zhao, J. Huang, Y. Liu, J. Shen, H. Wang, X. Yang, Y. Zhu, C. Li, Multimetallic Ni–Mo/Cu nanowires as nonprecious and efficient full water splitting c atalyst. J. Mater. Chem. A 5 (2017) 4207-4214. https://doi.org/10.1039/C6TA10749D.

[S15] L.-G. He, P.-Y. Cheng, C.-C. Cheng, C.-L. Huang, C.-T. Hsieh, S.-Y. Lu, ($Ni_xFe_yCo_{6-x-y}$)Mo_6C cuboids as outstanding bifunctional electrocatalysts for overall water splitting. Appl. Catal. B Environ. 290 (2021) 120049. https://doi.org/10.1016/j.apcatb.2021.120049.

[S16] F. Cai, L. Liao, Y. Zhao, D. Li, J. Zeng, F. Yu, H. Zhou, Large-current-stable bifunctional nanoporous Fe-rich nitride electrocatalysts for highly efficient overall water and urea

splitting. J. Mater. Chem. A 9 (2021) 10199-10207. https://doi.org/10.1039/D1TA00144B.

[S17] Y.-K. Li, G. Zhang, W.-T. Lu, F.-F. Cao, Amorphous Ni-Fe-Mo suboxides coupled with Ni network as porous nanoplate array on nickel foam: a highly efficient and durable bifunctional electrode for overall water splitting. Adv. Sci. 7 (2020) 1902034. https://doi.org/10.1002/advs.201902034.

[S18] A. Sahasrabudhe, H. Dixit, R. Majee, S. Bhattacharyya, Value added transformation of ubiquitous substrates into highly efficient and flexible electrodes for water splitting. Nat. Commun. 9 (2018) 2014. https://doi.org/10.1038/s41467-018-04358-7.

[S19] G. Xiong, Y. Chen, Z. Zhou, F. Liu, X. Liu, L. Yang, Q. Liu, Y. Sang, H. Liu, X. Zhang, J. Jia, W. Zhou, Rapid synthesis of various electrocatalysts on Ni foam using a universal and facile induction heating method for efficient water splitting. Adv. Funct. Mater. 31 (2021) 2009580. https://doi.org/10.1002/adfm.202009580.

[S20] F. Qin, Z. Zhao, M. K. Alam, Y. Ni, F. Robles-Hernandez, L. Yu, S. Chen, Z. Ren, Z. Wang, J. Bao, Trimetallic NiFeMo for overall electrochemical water splitting with a low cell voltage. ACS Energy Lett. 3 (2018) 546-554. https://doi.org/10.1021/acsenergylett.7b01335.

[S21] S. Hao, L. Chen, C. Yu, B. Yang, Z. Li, Y. Hou, L. Lei, X. Zhang, NiCoMo hydroxide nanosheet arrays synthesized via chloride corrosion for overall water splitting. ACS Energy Lett. 4 (2019) 952-959. https://doi.org/10.1021/acsenergylett.9b00333.

[S22] Y. Zhou, Z. Wang, Z. Pan, L. Liu, J. Xi, X. Luo, Y. Shen, Exceptional performance of hierarchical Ni-Fe (hydr)oxide@NiCu electrocatalysts for water splitting. Adv. Mater. 31 (2019) 1806769. https://doi.org/10.1002/adma.201806769.

[S23] D. S. Raja, H.-W. Lin, S.-Y. Lu, Synergistically well-mixed MOFs grown on nickel foam as highly efficient durable bifunctional electrocatalysts for overall water splitting at high current densities. Nano Energy 57 (2019) 1. https://doi.org/10.1016/j.nanoen.2018.12.018.

[S24] P. Chen, T. Zhou, M. Zhang, Y. Tong, C. Zhong, N. Zhang, L. Zhang, C. Wu, Y. Xie, 3D nitrogen-anion-decorated nickel sulfides for highly efficient overall water splitting. Adv. Mater. 29 (2017) 1701584. https://doi.org/10.1002/adma.201701584.

[S25] Y. Zhang, X. Xia, X. Cao, B. Zhang, N. H. Tiep, H. He, S. Chen, Y. Huang, H. J. Fan, Ultrafine metal nanoparticles/N-doped porous carbon hybrids coated on carbon fibers as flexible and binder-free water splitting catalysts. Adv. Energy Mater. 7 (2017) 1700220. https://doi.org/10.1002/aenm.201700220.

[S26] F. Yu, H. Zhou, Y. Huang, J. Sun, F. Qin, J. Bao, W. A. Goddard, S. Chen, Z. Ren, High-performance bifunctional porous non-noble metal phosphide catalyst for overall water splitting. Nat. Commun. 9 (2018) 2551. https://doi.org/10.1038/s41467-018-04746-z.

[S27] X. Yu, Z.-Y. Yu. X.-L. Zhang, Y.-R. Zheng, Y. Duan, Q. Gao, R. Wu, B. Sun, M.-R. Gao, G. Wang, S.-H. Yu, “Superaerophobic” nickel phosphide nanoarray catalyst for efficient hydrogen evolution at ultrahigh current densities. J. Am. Chem. Soc. 141 (2019) 7537-7543. https://doi.org/10.1021/jacs.9b02527.

[S28] W. Hao, R. Wu, H. Huang, X. Ou, L. Wang, D. Sun, X. Ma, Y. Guo, Fabrication of practical catalytic electrodes using insulating and eco-friendly substrates for overall water splitting. Energy Environ. Sci. 13 (2020) 102-110. https://doi.org/10.1039/C9EE00839J.

[S29] P. Wang, Y. Luo, G. Zhang, M. Wu, Z. Chen, S. Sun, Z. Shi, MnO_x-decorated nickel-iron phosphides nanosheets: interface modifications for robust overall water splitting at ultra-high current densities. Small 18 (2022) 2105803. https://doi.org/10.1002/smll.202105803.

[S30] B. Zhang, F. Yang, S. Liu, N. Wu, S. Che, Y. Li, Phosphorus doped nickel-molybdenum aerogel for efficient overall water splitting. Appl. Catal. B Environ. 298 (2021) 120494. https://doi.org/10.1016/j.apcatb.2021.120494.

[S31] L. Yu, I. K. Mishra, Y. Xie, H. Zhou, J. Sun, J. Zhou, Y. Ni, D. Luo, F. Yu, Y. Yu, S. Chen, Z. Ren, Ternary $Ni_{2(1-x)}Mo_{2x}P$ nanowire arrays toward efficient and stable hydrogen evolution electrocatalysis under large-current-density. Nano Energy 53 (2018) 492-500. https://doi.org/10.1016/j.nanoen.2018.08.025.